The Imaging Science Journal

ISSN: (Print) (Online) Journal homepage: https://www.tandfonline.com/loi/yims20

Conditional random field-recurrent neural network segmentation with optimized deep learning for brain tumour classification using magnetic resonance imaging

Geetha M, Prasanna Lakshmi K, Sajeev Ram Arumugam & Sandhya N

To cite this article: Geetha M, Prasanna Lakshmi K, Sajeev Ram Arumugam & Sandhya N (2023): Conditional random field-recurrent neural network segmentation with optimized deep learning for brain tumour classification using magnetic resonance imaging, The Imaging Science Journal, DOI: 10.1080/13682199.2023.2178611

To link to this article: https://doi.org/10.1080/13682199.2023.2178611

Published online: 03 Mar 2023.

THE IMAGING SCIENCE JOURNAL
https://doi.org/10.1080/13682199.2023.2178611

THE RPS ROYAL PHOTOGRAPHIC SOCIETY
Taylor & Francis Taylor & Francis Group

RESEARCH ARTICLE

Conditional random field-recurrent neural network segmentation with optimized deep learning for brain tumour classification using magnetic resonance imaging

Geetha M[a], Prasanna Lakshmi K[b], Sajeev Ram Arumugam[c] and Sandhya N[d]

[a]Department of Computer Science and Engineering, Chennai Institute of Technology, Chennai, India; [b]Department of Information Technology, Gokaraju Rangaraju Institute of Engineering and Technology, Hyderabad, India; [c]Department of Computer Science and Engineering, Sri Krishna College of Engineering and Technology, Coimbatore, India; [d]Department of CSE, VNR Vignana Jyothi Institute of Engineering and Technology, Hyderabad, India

ABSTRACT

Brain tumour is one of the most dreadful kinds of tumour caused by the uncontrolled increase in the cells inside the skull. Clinically, brain tumour is diagnosed using different imaging methods, among which Magnetic Resonance Imaging (MRI) is the most extensively utilized technique. The proposed work intends to develop a Deep Learning (DL) based approach for segmenting and classifying to diagnose brain tumours from the brain MRI. This work proposes two novel approaches: (i) tumour segmentation technique using Conditional Random Field-Recurrent Neural Network (CRF-RNN), whose weights are adapted with the help of the novel Chronological Artificial Hummingbird Algorithm (CAHA). (ii) A brain tumour classification scheme using LeNet. Further, an optimization algorithm called Chronological Artificial Vultures Optimization (CAVO) is proposed for the weight optimization of the LeNet. It is observed that the devised model attained higher values of specificity, sensitivity, and accuracy of 0.938, 0.941, and 0.930.

ARTICLE HISTORY
Received 31 October 2022
Accepted 6 February 2023

KEYWORDS
Brain tumour; segmentation; classification; deep learning; optimization; malignant; Recurrent Neural Network; Magnetic Resonance Imaging

Introduction

MRI is a forefront strategy in medical imaging employed to ascertain the functional and structural condition of the various organs and tissues in the body [1]. MRI has transformed the field of medical imaging, causing a revolution in medical research by offering non-invasive and repeatable quantifications of the function and structure of tissues. It is a highly adaptable imaging modality as the image's sensitivity to the various aspects of the tissues can be altered broadly by adjusting the time of collecting MR signals [2–4]. MRI is an advanced imaging technique that can effectively evaluate the tumours found in brain images. MRI images are employed in treating brain tumours in the advanced stages [5–7]. A tumour refers to the uninhibited growth of cancerous cells in any region of the body. The tumour classification is performed considering the various features of the tumourous region and the associated inconsistent treatments. The brain tumour is one of the most dangerous and painstaking diseases among all tumour types, requiring precise assessment by medical professionals to accurately categorize the tumour [8]. Brain tumour denotes the unrestrained expansion of the cells in the brain. Generally, cells develop and enlarge, and later, after a brief duration, they die and are replaced by new cells. But occasionally, the cells thrive for longer than intended owing to certain complications and begin to multiply, leading to a large cellular mass. The cellular mass thus generated grows at a disturbing rate forming a massive mass hampering the regular functioning of the brain [9].

Brain tumours emerge from the cells around the meninges (the brain membranes), nerves, or glands in the brain. They can unambiguously affect and damage the brain cells by causing increased pressure in the skull's interior [10]. Brain tumour treatment can be performed if the tumour is identified at an initial stage. Brain tumours can be classified as malignant and benign, wherein the malignant tumour is devoid of any constant and organized uniformity. Generally, benign tumours have non-existent and rigid uniformity [11]. Further, brain tumours can be categorized as Pituitary, Glioma, and Meningioma. Meningiomas are commonly non-cancerous tumours that most commonly form in the thin walls surrounding the brain. Pituitary tumours are non-cancerous and originate in the pituitary glands [12]. Conversely, Gliomas are the main class of brain tumours that emerge from the glial cells and penetrate the neighbouring brain tissues, and they can be categorized into High-Grade Glioma (HGG) and Low-Grade Glioma (LGG). LGG has a slower growth rate, and with the

CONTACT M. Geetha mgeetha@citchennai.net Department of Computer Science and Engineering, Chennai Institute of Technology, Chennai, India

help of appropriate treatment, the survival rate of the affected individuals can be prolonged. The successful treatment of brain tumours depends on the evaluation of the progression rate of the disease, considering the accuracy of the neuroimaging modalities [13]. Clinically, brain tumour is diagnosed based on the analysis of the imaging data of tumour images. Examining the tumour images is the most significant step in identifying the individual's condition. But, the accuracy of the analysis depends on various factors, such as visual fatigue, variations in the experiences, and knowledge of the medical professionals [14–16]. Thus, the most significant process in treating brain tumours is to decide the detection process [17]. MRI can offer numerous data [18, 19] concerning the position, dimensions, and shape of the body's organs and tissues without harmful ionizing radiation. Further, the efficiency of the diagnosis is greatly enhanced, as the images are highly precise and clear and can be effectively used for localizing the lesions [20].

Brain tumour categorization is highly demanding owing to the inherent high variations in the characteristics of MRI, such as uncertainty in the determination of the segmented areas, classification, segmentation, area calculation, tumour detection, and tumour shape and size variations [21–23]. Image segmentation is the most important process in interpreting the image as it aids in area computation and feature extraction, which is highly beneficial in several real-time applications [24–26]. Segmentation can be utilized in several areas, such as image registration, surgical planning, atlas matching, tumour localization, delineation of blood cells, tissue categorization, tumour volume estimation, etc [27–29]. A crucial process in policing oncology therapy is detecting tumours precisely and accurate morphological estimation [30–32]. Several approaches to identifying brain tumours exist, such as Machine Learning (ML) [33, 34], region growing [35], fuzzy clustering [36], and level set detection [37–39]. Most ML schemes for classifying brain tumours include random forest, expectation-maximization, Naïve Bayes, support vector machine (SVM), decision trees, and K-Nearest Neighbours (KNN) [12, 40]. Over the last few years, DL methods have been employed for categorizing brain tumours automatically by extracting the features directly from the image [41]. DL is a branch of ML, which provides systems the ability to estimate and learn the representations in the data, enabling them to make better decisions in various fields [42–45]. DL techniques act as the main computational intelligence approaches and have been widely utilized for the classification of images. In particular, the Convolutional Neural Network (CNN) is most commonly used in assessing medical images and offers high accuracy [46–48].

This work presents an efficient DL technique for classifying brain tumours based on MRI scans of the brain. The presented CAVO-LeNet for brain tumour categorization is implemented using the following phases: input acquisition, preprocessing, segmentation of tumour, feature mining, and finally, classification. Here, the input MRI is initially subjected to anisotropic filtering, followed by segmentation using the CRF-RNN with weights optimized using the CAHA. After tumour segmentation, the most relevant features are extracted and applied to the LeNet to classify brain tumours as Meningiomas, Gliomas as well as Pituitary tumours, wherein, the weight parameter of the LeNet is optimized with the presented CAVO algorithm.

The main contributions of this paper are listed as follows:

- *Introduced CAHA-CRF-RNN for tumour segmentation*: A novel strategy for segmenting the tumours from the filtered MRI images is proposed using CRF-RNN, whose weights and biases are optimized using the devised CAHA. Here, the CAHA is formed by modifying the Artificial Hummingbird Algorithm (AHA) based on the Chronological concept to improve the optimization process.
- *Devised CAVO-LeNet for brain tumour classification:* Here, classification is performed by proving the most relevant features of the input MRI images to the LeNet. Further, the classification process is optimized by modifying the learning parameters of the LeNet with the presented CAVO algorithm. The CAVO algorithm is formulated by modifying the CAHA based on the African Vultures Optimization Algorithm (AVOA).

The arrangement of this work embodies that section 2 details the associated works of brain tumour classification, section 3 elucidates the devised CAVO-LeNet for classifying brain tumour, the experimental outcomes and assessment is highlighted in section 4, and in section 5, the paper is concluded.

Motivation

The prognosis and proper treatment of the brain tumour can enhance the lifetime of the individuals and reduce the mortality rate. Several automated approaches to brain tumour detection have been developed in the past, and with the advent of DL approaches, the problem of classifying medical images has been addressed effectively. However, classifying brain tumours is highly complex due to the multiple processes involved, and utmost care must be taken in executing each process to enhance accuracy. This section elucidates a few of the available brain tumour detection schemes and provides a

review of the merits and challenges which stimulated the creation of the presented classification technique.

Literature review

Numerous works have dealt with the problem of brain tumour detection and categorization, which are described in this section.

Deep learning-based methods

Hashemzehi, R. et al. [12] proposed a Hybrid CNN-Neural Autoregressive Distribution Estimation (NADE) model for identifying brain tumours. The hybrid approach was implemented using three main phases: estimating the density, exploiting the feature, and classifying. This technique effectively smoothened the brain boundary and removed unwanted features. Additionally, it was effective in handling the problems associated with imbalanced datasets. Still, the approach did not consider improving the system's performance by obtaining extra features utilizing pre-processing steps, like common filter and segmentation. Rehman, A., et al. [49] presented 3D CNN and Correlation-based along Feed-Forward Neural (CbFNN) technique for extracting and classifying brain tumours. Here, the 3D CNN model was employed to mine tumours from the MRI scans, followed by applying transfer learning for classification. Feature mining was performed based on the pre-trained CNN model Visual Geometry Group 19 (VGG19), and the optimal feature was selected using the CbFNN technique. This scheme was highly effective in segmenting tumours from low-contrast tumour regions, but the system's performance is limited by high classification time. Rajinikanth, V. et al. [50] devised a Deep Learning Architecture (DLA) with a customized VGG19 network for detecting brain tumour. Here, the DLA was employed for the classification process, wherein the softmax classifier was replaced by DLAs, like decision trees, SVM-Radial Basis Function (RBF), SVM-Linear, and KNN classifiers. The customized VGG was devised by combining the deep and handcrafted features and sorting the features using the Principal Component Analysis (PCA). The sorted features were subjected to fusion using the serial concatenation approach, and finally, the feature vector was employed to improve the classification accuracy. This approach effectively enhanced the accuracies without depending on the image modalities; although the technique failed to classify the tumours into LGG/HGG.

Chetana Srinivas, *et al.* [51] established transfer learning-based CNN technique for automatically identifying the tumour cells in brain. In this approach, in every phase, the integral tuning was considered. This technique offered high prediction accuracy, but it was undergo overfitting problems.

Machine learning-based methods

Chaudhary, A. and Bhattacharjee, V., [9] developed a K-means clustering & Discrete Wavelet Transform (DWT) for detecting and classifying the brain tumour. This scheme employed a K-means clustering technique for segmentation, followed by the utilization of QWT for extracting features, and lastly, SVM performed classification. This scheme successfully predicted the tumour's size and shape; however, the technique suffered from the lack of perfection in effectively detecting tumours owing to the aberrations in different processing schemes. Sharif, M. et al. [52] presented an Extreme Learning Machine (ELM)-based classifier for identifying brain tumours. The ELM-based classifier utilized Triangular Fuzzy Median Filtering (TFMED) to enhance the images, and segmentation was performed with the help of fuzzy-based unsupervised clustering. Later, the Gabor and Similar Texture (ST) features were obtained and fed to the ELM for classification. This methodology successfully identified the tumour growth region with minimal computational complexity but it was unsuccessful in performing the detection of all sub-tumoural areas. Deb, D. and Roy, S., [53] developed a Hybrid Adaptive fuzzy deep neural network (AFDNN) with the frog leap algorithm for classifying brain tumours. This technique extracted the Gray Level Co-Occurrence Matrix (GLCM) features from the filtered input image, and then the features were subjected to the AFDNN for classifying the images. The frog leap algorithm was utilized for optimizing the AFDNN. The abnormal images were fed to the segmentation process using the Adaptive Squirrel Search Algorithm (ASSA). The hybrid AFDNN effectively eliminated the errors in classification and was appropriate for images with noise; however, the technique failed to minimize the computational complexity. Amin, J. et al. [54] Long Short-Term Memory (LSTM)-based learning scheme for automatically classifying brain images. The LSTM approach utilized a Gaussian filter and N4ITK filter to enhance the input MRI image quality. These images are used as the input of the LSTM for performing classification. This approach accurately classified HGG and LGG and it was effective in detecting stroke. However, the method did not consider the subtumoural area's classification and failed to quantify the tumour severity level.

Optimization-based methods

Sharma, A. K. et al. [55] devised an Enhanced Watershed Segmentation (EWS) algorithm based modified ResNet50 approach to detect brain tumours. This approach employed the EWS algorithm for segmentation, wherein the EWS algorithm comprised three basic steps: morphological restoration, markup extraction, and mark-based transformation. The segmented image was augmented and then applied to the ResNet50 for classification. Though this method

Table 1. Review based on conventional approaches.

Reference	Methods	Merits	Demerits
Hashemzehi, R. et al. [12]	Hybrid CNN-NADE	• It effectively smoothened the brain boundary and removed unwanted features. • it was effective in handling the problems associated with imbalanced datasets	• Did not consider improving the system's performance by obtaining extra features.
Chaudhary, A. and Bhattacharjee, V. [9]	K-means clustering + DWT	• It successfully predicted the tumor's size and shape.	• It suffered from the lack of perfection.
Rehman, A., et al. [49]	3D CNN-CbFNN	• It was highly effective in segmenting tumors from the low-contrast tumor region	• It required high classification time.
Rajinikanth, V. et al. [50]	DLA	• It effectively enhanced the accuracies without depending on the image modalities	• It failed to classify the tumors into LGG/HGG.
Sharif, M. et al. [52]	ELM-based classifier	• It identified the tumor growth region with minimal computational complexity.	• It was unsuccessful in performing the detection of all sub-tumoral areas.
Deb, D. and Roy, S., [53]	AFDNN	• It effectively eliminated the errors in classification	• It failed to minimize the computational complexity.
Amin, J. et al. [54]	LSTM-based learning scheme	• It accurately classified HGG and LGG.	• It did not consider the subtumoral area's classification.
Sharma, A.K. et al. [55]	EWS algorithm	• It accurately identified the tumor location by determining the actual location of boundary pixels	• It failed to consider multimodal images for classification.
Chetana Srinivas, et al. [51]	transfer learning-based CNN	• It offered high prediction accuracy.	• It was undergo overfitting problems.

accurately identified the tumour location by determining the actual location of boundary pixels; it failed to consider multimodal images for classification.

The review based on the conventional approaches is described in Table 1.

Devised CAVO-Lenet for brain tumour classification

The presented CAVO-LeNet for categorizing brain tumours is presented in Figure 1. Initially, the input MRI images are acquired from the database and fed to the anisotropic filtering [56] for preprocessing, wherein the noises present in the MRI images are minimized without eliminating the relevant edges and other aspects of the image. Later, the filtered image is subjected to the CRF-RNN [57] for segmenting the tumour. Here, the appropriate weights of the CRF-RNN are determined with the CAHA, devised by adapting the AHA [58] based on the chronological concept. Once the tumour is segmented using the CAHA-CRF-RNN, the most relevant features in the image, such as CNN features [59] and statistical features, like mean, variance, standard deviation, energy, and correlation [60], and texture features, such as spider local image features (SLIF) [61], Pyramid Histogram of Oriented Gradients (PHOG) [62] and Local Vector Pattern (LVP) [63] are extracted. After that, classification is executed using LeNet [64], where brain tumours are categorized as Gliomas, Meningiomas, and Pituitary tumours. Moreover, the CAVO algorithm is proposed for adapting the learning parameters of the LeNet, wherein the CAVO algorithm is created by modifying the proposed CAHA using the AVOA [65]. The process of classifying brain tumours with the presented CAVO-LeNet is explained in the ensuing sections.

Image acquisition

A dataset Q containing a total count of count of input MRI images is considered, and it can be expressed as,

$$Q = \{Q_1,\ Q_2 \cdots Q_k \cdots Q_z\} \tag{1}$$

Here, Q_k designates the k^{th} input image in the dataset that is subjected to the next pre-processing stage.

Pre-processing

The primary step in the classification process is to pre-process the input MRI images to prepare the MRI images for the classification process. Here, anisotropic filtering [56] is employed to remove the images' noises

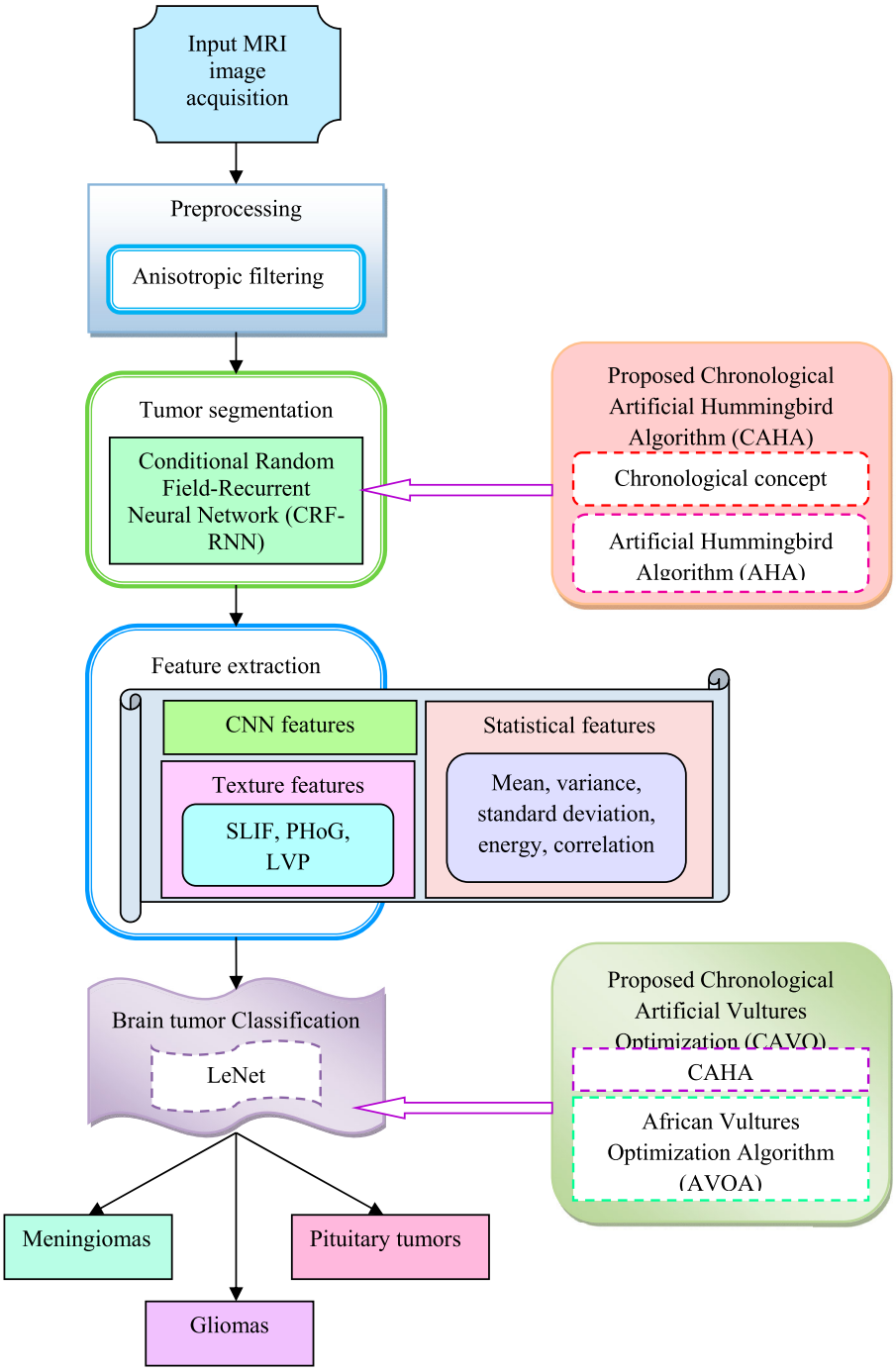

Figure 1. Schematic view of the presented CAVO-LeNet for classifying brain tumor.

without affecting the image's other important aspects. Generally, medical images are highly impacted by noise, which deteriorates the performance of image processing systems. Hence, to overcome this issue, filtering is required. The anisotropic filter uses the principle of diffusion on the intensity of the pixels. The anisotropic diffusion process is given by,

$$\frac{\partial Q_k}{\partial t} = div(a(x, y, t)\nabla Q_k) = \nabla a \cdot \nabla Q_k + a(x, y, t)\Delta Q_k \quad (2)$$

where, $a(x, y, t)$ specifies the diffusion coefficient, Δ denotes the Laplacian operator, ∇Q_k is the image gradient. $Q_k(., 0)$ indicates the input image, and, *div* symbolizes the divergence function, and $Q_k(., t)$ denotes the output image and let it be denoted as B_k, which is provided to the segmentation stage.

Tumour segmentation

Tumour segmentation is executed using the CRF-RNN [57], which is applied with the anisotropic filtered output B_k. The segmentation process splits an image into well-defined regions depending on the similarity attributes of the pixels contained. Segmentation is carried out by allocating values to all the pixels in the image and the pixels with similar values reveal a

specific feature. The segmented regions disclose highly significant details contained in the image. Here, the tumour region is segmented using the CRF-RNN, whose weight parameters are appropriately determined with the developed CAHA. The proposed CAHA algorithm is developed using the Chronological concept to modify the AHA [58]. The process of segmentation is detailed in the sections ensuing.

Architecture of CRF-RNN

The pre-processed image $Q_k(., t)$ is applied to the CRF-RNN [57, 66] for segmenting the tumour regions. Segmentation normally requires labelling of the image at pixel levels, but the DL approaches mainly suffer from the restricted ability to demarcate visual objects. This can be effectively overcome by using the CRF-RNN, wherein mean-field approximate inference and Gaussian pairwise potentials are used as RNN with CRF. CRF is employed for formulating the label assignment issue as an interference model based on probability. CRF interference has the ability in refining the coarse and weak label estimations to provide the segmented image with a sharp boundary. Consider the filtered image $Q_k(., t)$ has a total of N pixels , wherein each pixel is considered to have a label $c_l \in D = \{1, 2, .., l\}$, with D indicating the potential labels. The energy parameter of the CRF is expressed as,

$$F(c) = \sum_{l} \xi_u(c_l) + \sum_{l<m} \xi_{pr}(c_l, c_m) \tag{3}$$

Here, $\xi_{pr}(c_l, c_m)$ indicates the pairwise potentials used to represent the cost of allocating label c_l and c_m to the l^{th} and m^{th} pixels, respectively, and $\xi_u(c_l)$ is the unary potential, which is obtained by,

$$\xi(c_1) = -\log B(l) \tag{4}$$

where, $B(l)$ represents the probability of the l^{th} pixel being contained in the hippocampus. The pairwise potential is computed using,

$$\xi_{pr}(c_l, c_m) = \lambda(c_l, c_m)\left[d^1 \exp\left(-\frac{|e_l - e_m|^2}{2\sigma_\eta^2}\right)\right.$$

$$\left. + d^2 \exp\left(-\frac{|e_l - e_m|^2}{2\sigma_v^2} - \frac{|f_l - f_m|^2}{2\sigma_\rho^2}\right)\right] \tag{5}$$

Here, $\lambda(c_l, c_m) = \{1 \text{ if } c_l \neq c_m, \text{ else } 0\}$ represents a modest label compatibility parameter to castigate the neighbouring pixels with various labels, $|e_l - e_m|$, which relies on the location of the pixels and $|f_l - f_m|$ is dependent on colours, d^1, d^2 regulates the impact of two terms, and σ_η, σ_v, σ_ρ are used to adjust the impact of multiple features, like colour, and location. The RNN is reformulated based on mean-fieldCRF inference. Further, bilateral and Gaussian space filters are applied to approximate the mean field during each iteration. The mean-field iteration procedure is established in five phases: message passing, reweighting, transforming the compatibility, and addition of unary potentials and normalizing. The process is repeated for the total of R number of iterations. CRF-RNN can significantly enhance the segmentation ability per pixel colour and location relationship. The architectural view of the CRF-RNN is exhibited in Figure 2.

Fitness calculation

Though the segmentation accuracy can be effectively improved using the CRF-RNN, the efficiency can be further improved by segmenting the hippocampus edges more precisely by using an edge-aware loss function. This loss function integrates the information acquired from the previous edges of the annotated images, and this is computed as,

$$EL_{edge} = -\sum_{l} A(l) \log (B(l)).e_g(l) \tag{6}$$

Here, $A(l)$ indicates the probability of the l^{th} pixel being present in the background.

$$e_g(l) = e_f(l) + e_0.\Theta\left(\sqrt{C_1^2(i) + C_2^2(i) + C_3^2(i)} > \alpha\right) \tag{7}$$

Here, the term $e_f(l)$ underscores classes having the lowest frequency to handle the issue of class imbalance and is pre-determined considering the average frequency of all classes contained in the image. The second term in the equation provides significance to the edge pixel for enhancing the segmenting the contour. The horizontal, diagonal, and vertical gradients of the l^{th} pixel are indicated by , and the pixel is contemplated as an average pixel when the value of $\sqrt{C_1^2(i) + C_2^2(i) + C_3^2(i)}$ is greater than the threshold α. $\Theta(*)$ represents the indicator function.

Training of CRF-RNN with the CAHA

This section details the tuning of the weight parameters of the CRF-RNN employed for segmenting the tumour area from the filtered image using the developed CAHA. The CAHA is formulated by utilizing the chronological concept to modify the guided foraging strategy of the AHA [58]. The AHA algorithm is based on the smart foraging tactics and special abilities of the hummingbird, the smallest and smartest bird. This algorithm imitates three kinds of search tactics, like migrating, territorial foraging, and guided foraging, and three classes of flight patterns, omnidirectional, axial, and diagonal flights. Further, a significant constituent named the visit table is presented for implementing the memory of the hummingbird while discovering and choosing food sources. The hummingbirds choose a suitable food source based on the various properties of the food source, like last time the flower is visited, quality and refilling rate of nectar, and the content of distinct

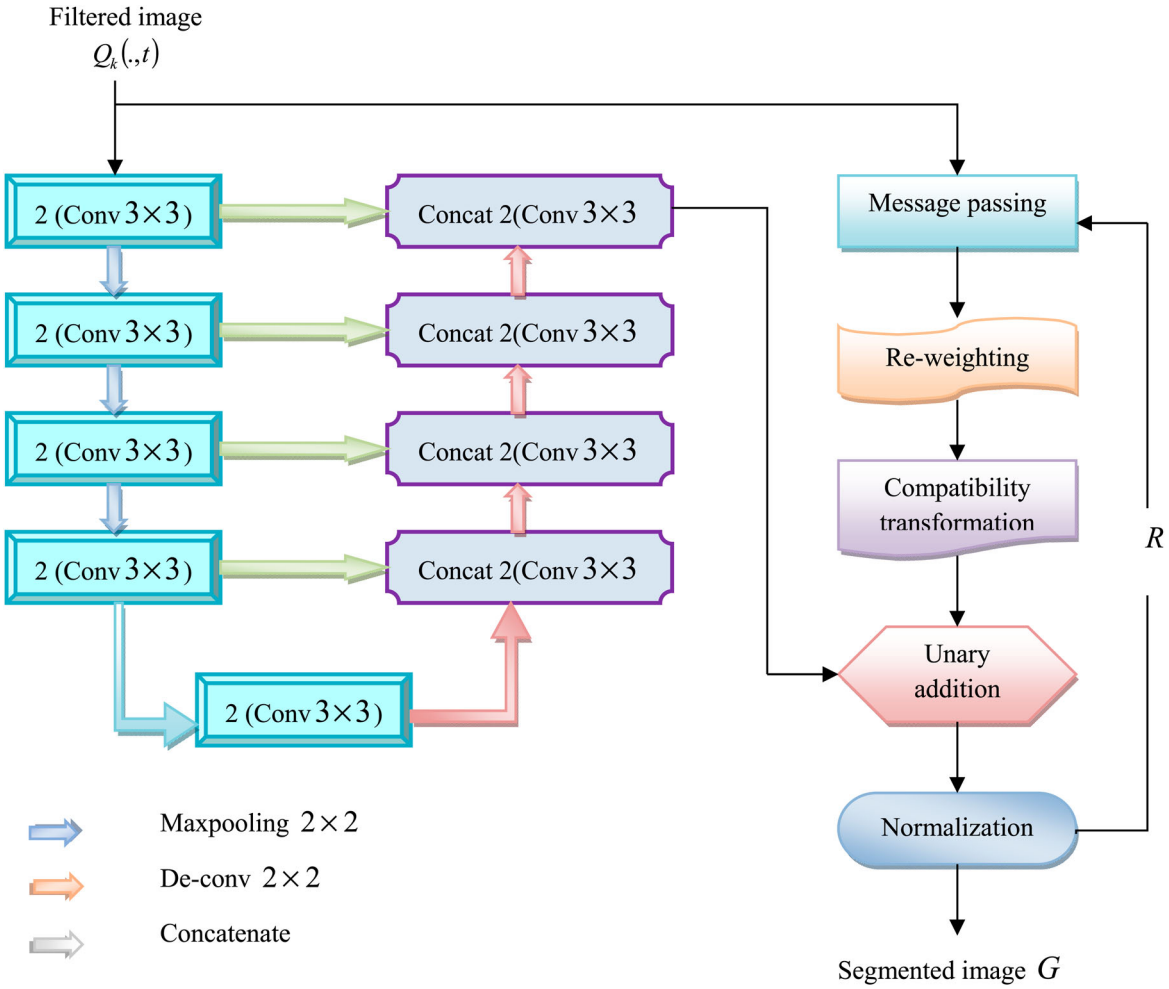

Figure 2. Architectural design of the CRF-RNN.

flowers. The visit table contains the recorded visit level of the various hummingbirds to the food source. The AHA offers the advantage of achieving global optimum with minimal computational complexity. However, the AHA failed to handle multi-objective issues, and enhance the local search behaviours. To tackle this issue, the AHA algorithm is modified considering the chronological concept to generate the CAHA, for tuning the weights of the CRF-RNN. The chronological concept employs the prior and current values of the iteration to improve the optimization. The algorithmic steps of the presented CAHA are detailed in the succeeding section.

Step 1: Initialization

Initially, a population H of hummingbirds K is initialized which are located on K food sources, which is denoted by,

$$H_s = lw + o \times (up - lw), \qquad s = 1, 2, \ldots, K \quad (8)$$

Here, o is an arbitrary vector in the range [0, 1], up and lw characterizes the highest and lowest limits of the problem with E dimension, and is the location of the s^{th} food source or the solution of the issue to be addressed. The visit table is also initiated in the primary step, which is expressed as,

$$VT_{v,w} = \begin{cases} 0 & if\ v \neq w \\ null & v = w \end{cases}; \ v = 1, \ldots, K, \ w = 1, \ldots, K \quad (9)$$

The, value of $VT_{v,w}$ is set to 0 for in case the v^{th} hummingbird has visited the w^{th} food source in the present iteration and visit table $VT_{v,w}$ is set to a value of *null* if $v = w$, and this specifies that the hummingbird v is feeding on the w^{th} source.

Step 2: Fitness evaluation

The fitness of the solution is evaluated using the edge-aware loss function, which is specified using equation (6), wherein the best solution is obtained by considering the minimum loss.

Step 3: Guided foraging

The hummingbird inclines to explore the food source with a maximum visited time and a high volume of nectar, which denotes the target had an enhanced frequency of refilling the nectar. The target food source with a high volume of nectar is determined by using the guided foraging technique. In this phase, the hummingbird approaches the food source using three categories of flight skills, such as axial, omnidirectional, and diagonal. The hummingbird

glides alongside the coordinate axis in the axial flight and this skill is modelled as,

$$L_v = \begin{cases} 1 & if\ v = randi([1, E]) \\ 0 & else \end{cases},\ v = 1,\ \ldots.,\ E \quad (10)$$

Here, *randi*([1, *E*]) produces an arbitrary integer in the range [1, *E*]. The diagonal flight permits the hummingbird to fly from a corner to the opposite corner of the rectangle, and this is expressed as follows,

$$L_v = \begin{cases} 1 & if\ v = M(w),\ w \in [1, h],\ M = randperm(h),\ h \in [2, \lceil o_1.(E-2) \rceil + 1] \\ 0 & else \end{cases},\ v = 1,\ \ldots.,\ E \quad (11)$$

where, *randperm*(*h*)generates an arbitrary permutation from 1 to *h*. The omnidirectional flight represents that the hummingbird can fly in any possible direction along the three axes and is given by,

$$L_v = 1,\ v = 1,\ \ldots,\ E \quad (12)$$

The hummingbird utilizes all these capabilities to visit its chosen food source to determine the candidate solution and the guided foraging characteristics can be expressed using the equation given below.

$$P_v(t+1) = U_{v,tar}(t) + \beta \cdot L \cdot (U_v(t) - U_{v,tar}(t)) \quad (13)$$

Here, $\beta \sim N(0, 1)$ and $U_v(t)$ indicates the of v^{th} food source location at time t, β symbolizes the guided factor and $U_{v,tar}(t)$ denotes the target food source location visited by the v^{th} hummingbird, and $N(0, 1)$ indicates the normal distribution. The location of the v^{th} food source is modified based on the following expression,

$$U_v(t+1) = \begin{cases} U_v(t) & if\ f(U_v(t) \le f(P_v(t+1))) \\ P_v(t+1) & f(U_v(t) > f(P_v(t+1))) \end{cases} \quad (14)$$

wherein, $f(.)$ indicates the fitness measure given by equation (6). Now, consider the criteria $f(U_v(t) > f(P_v(t+1)))$ in the above equation, we get,

$$U_v(t+1) = P_v(t+1) \quad (15)$$

Substituting equation (13) in equation (15), we get,

$$U_v(t+1) = U_{v,tar}(t) + \beta \cdot L \cdot (U_v(t) - U_{v,tar}(t)) \quad (16)$$

$$U_v(t+1) = U_{v,tar}(t) + \beta \cdot L \cdot U_v(t) - \beta \cdot L \cdot U_{v,tar}(t) \quad (17)$$

$$U_v(t+1) = U_{v,tar}(t)(1 - \beta \cdot L) + \beta \cdot L \cdot U_v(t) \quad (18)$$

Using the chronological concept,

$$U_v(t+1) = \frac{U_v(t+1) + U_v(t+1)}{2} \quad (19)$$

At t^{th} iteration,

$$U_v(t) = U_{v,tar}(t-1)(1 - \beta \cdot L) + \beta \cdot L \cdot U_v(t-1) \quad (20)$$

Applying equation (20) in equation (18),

$$U_v(t+1) = U_{v,tar}(t)(1 - \beta \cdot L) + \beta \cdot L \cdot (U_{v,tar}(t-1)(1 - \beta \cdot L) + \beta \cdot L \cdot U_v(t-1)) \quad (21)$$

$$U_v(t+1) = U_{v,tar}(t)(1 - \beta \cdot L) + \beta \cdot L \cdot (1 - \beta \cdot L)U_{v,tar}(t-1) + \beta^2 \cdot L^2 \cdot U_v(t-1) \quad (22)$$

$$U_v(t+1) = (1 - \beta \cdot L)(U_{v,tar}(t) + \beta \cdot L \cdot U_{v,tar}(t-1)) + \beta^2 \cdot L^2 \cdot U_v(t-1) \quad (23)$$

Now, applying equation (18) and equation (23) in equation (19),

$$U_v(t+1) = \frac{1}{2}\begin{bmatrix} U_{v,tar}(t)(1 - \beta \cdot L) + \beta \cdot L \cdot U_v(t) + (1 - \beta \cdot L)(U_{v,tar}(t) \\ + \beta \cdot L \cdot U_{v,tar}(t-1)) + \beta^2 \cdot L^2 \cdot U_v(t-1) \end{bmatrix} \quad (24)$$

$$U_v(t+1) = \frac{1}{2}\begin{bmatrix} U_{v,tar}(t)(1 - \beta \cdot L) + \beta \cdot L \cdot U_v(t) + (1 - \beta \cdot L)U_{v,tar}(t) \\ + \beta \cdot L \cdot (1 - \beta \cdot L)U_{v,tar}(t-1) + \beta^2 \cdot L^2 \cdot U_v(t-1) \end{bmatrix} \quad (25)$$

$$U_v(t+1) = \frac{1}{2}[2U_{v,tar}(t)(1 - \beta \cdot L) + \beta \cdot L \cdot U_v(t) + \beta \cdot L \cdot (1 - \beta \cdot L)U_{v,tar}(t-1) + \beta^2 \cdot L^2 \cdot U_v(t-1)] \quad (26)$$

Here, $U_v(t)$ and $U_v(t+1)$ are the location of the v^{th} solution during the t and $(t+1)^{th}$ iterations. Once the hummingbird finds its selected food, the visit table is upgraded, so as to enable it to determine the time duration of the last visit.

Step 4: Territorial foraging

Once the target food source is visited, the hummingbird feeds on the nectar, after which it explores a new source rather than visiting the different prevailing sources. Thus, the bird moves to the surrounding areas in its terrain, wherein a new food source is determined to be superior to the prevailing source. This behaviour is formulated as,

$$P_v(t+1) = U_{v,tar}(t) + X \cdot L \cdot U_v(t) \quad (27)$$

wherein, X indicates the territorial aspect based on the normal distribution. The Visit table is updated after the conclusion of the territorial foraging stage.

Step 5: Migration foraging

While a food shortage occurs in an area, which is frequented by the hummingbird, it migrates to a farther place in search of food. The hummingbird at the

food source has a minimal rate of refilling of nectar shifts to a new random location, when the total iterations exceed the pre-decided value, and this characteristic is depicted as,

$$U_{worse}(t+1) = lw + o \times (up - lw) \tag{28}$$

where, $U_{worse}(t+1)$ signifies the food source with the worst nectar refilling rate.

Step 6: Evaluate the feasibility

The feasibility of the solution generated is analyzed considering the fitness parameter computed using equation (6). If any solution generated has a superior fitness to the current one, the obtained solution is contemplated as the best solution.

Step 7: Termination

The entire process is replicated until the best solution is obtained. The pseudocode of CAHA is exhibited in algorithm 1.

Algorithm 1. Pseudocode of CAHA

Pseudocode of CAHA
Initialization
For v^{th} hummingbird ($v = 1{:}K$)
Do $H_s = lw + o \times (up - lw)$
For w^{th} food source ($w = 1{:}K$) **Do**
If $v \neq w$
Then $VT_{v,w} = 1$,
Else $VT_{v,w} = null$,
End if
End for
End for
While $t \leq t_{\max}$ Do;
For v^{th} hummingbird ($v = 1{:}K$), **Do**
If *rand* ≤ 0.5 **then**
If $o < 1/3$ **then** execute equation (10)
Else if $o \geq 1/3$ **then** execute equation (11)
Else execute equation (12)
End if
End if
Execute equation (26)
If $f(P_v(t+1)) < f(U_v(t))$
Then $U_v(t+1) = P_v(t+1)$
For w^{th} food source ($w = 1{:}K$), $w \neq tar$, v **Do**
Update Visit table $VT_{v,w} = VT_{v,w} + 1$
End for
$VT(v, tar) = 0$,
For w^{th} food source ($w = 1{:}K$) **Do**
Update Visit table $VT_{v,w} = \max_{\chi \in K, \chi \neq w} (VT_{\chi,w}) + 1$
End for
Else
For w^{th} food source ($w = 1{:}K$), $w \neq tar$, v **Do**
Update Visit table $VT_{v,w} = VT_{v,w} + 1$
End for

End
Else
Execute equation (27)
If $f(P_v(t+1)) < f(U_v(t))$
Then $U_v(t+1) = P_v(t+1)$
For w^{th} food source ($w = 1{:}K$), $w \neq v$ **Do**
$VT_{v,w} = VT_{v,w} + 1$
End for
For w^{th} food source ($w = 1{:}K$) **Do**
$VT_{v,w} = \max_{\chi \in K, \chi \neq w} (VT_{\chi,w}) + 1$
End for
Else
For w^{th} food source ($w = 1{:}K$), $w \neq v$ **Do**
$VT_{v,w} = VT_{v,w} + 1$
End for
End if
End if
End for
If mod(t, $2K$) $== 0$,
Then execute equation (28)
For w^{th} food source ($w = 1{:}K$), $w \neq v$ **Do**
$VT_{worse,w} = VT_{worse,w} + 1$
End for
For w^{th} food source ($w = 1{:}K$) **Do**
$VT_{w,worse} = \max_{\chi \in K, \chi \neq w} (VT_{\chi,w}) + 1$
End for
End if
End while

Thus, the segmented brain is acquired using the CAHA-CRF-RNN is denoted as G, wherein the weights of the CRF-RNN are adapted based on CAHA. The modification of the AHA using the chronological concept has effectively enhanced the local search of the AHA, thus achieving improved efficiency.

Feature extraction

The segmented tumour $G$is forwarded to the feature mining step for selecting the various features in the image that offers a unique description of the image. The image contains a substantial quantity of information, among which all details are not needed; hence, the most salient features that completely describe the image are extracted to minimize the efforts required to analyze the image. Here, the most relevant features in the image are such as CNN features and statistical features, like mean, variance, standard deviation, energy, and correlation, and texture features, such as SLIF [67], PHOG [62], and LVP [63] are extracted. These features are elucidated in the subsequent sections.

CNN features

CNN [59] is a feed forward Artificial Neural Network (ANN) that encompasses three categories of layers: convolutional (conv), pooling, and Fully Connected (FC) layers. The conv layer is accountable for determining the relevant features contained in the image. The pooling layers minimize the overall count of network parameters, thereby effectively reducing overfitting and computational burden. The features obtained from the preceding conv layers are integrated by the FC layer. The CNN employs two significant processes, local connectivity, and collective weights, to decrease memory imprint and enhance efficiency. Consider the obtained CNN features to be represented as S_1.

Statistical features

Several statistical features, like mean, variance, standard deviation, energy, and correlation[60], are extracted from the segmented image, and these features are explained as follows.

Mean: This feature is employed for determining the involvement of all the individual pixels in the full image and is formulated as,

$$S_2 = \frac{1}{\beta}\sum_{i=1}^{\beta} Y_i \tag{29}$$

wherein, Y_i specifies the intensity of the i^{th} pixel, and β designates the overall count of pixels in the segmented image.

Variance: It is utilized to identify the variation of every pixel from the centre or the adjacent pixels, and can be calculated with the following expression,

$$S_3 = \frac{1}{\beta}\sum_{i=1}^{\beta} (Y_i - S_2)^2 \tag{30}$$

wherein, S_2 designates the mean feature.

Standard deviation: This quantifies the variations in intensities of the gray level of the image and is measured by taking the square root of the variance and is denoted as S_4.

Correlation: The correlation feature determines the linear dependence between the grayscale value in the images, which is illustrated as,

$$S_5 = \sum_{i=0}^{\psi-1}\sum_{j=0}^{\psi-1} \frac{(i - S_{1i})(j - S_{1j})}{\sqrt{(S_{i4}^2)(S_{j4}^2)}} \tag{31}$$

where, ψ designates the count of gray levels in the segmented images.

Energy: The energy parameter is essential in determining the similarity between the pixels in the image and is computed using the following equation,

$$S_6 = \sqrt{\sum_{i=0}^{\psi-1}\sum_{j=0}^{\psi-1} W(i,j)^2} \tag{32}$$

Here, $W(i, j)$ signifies the normalized gray scale value of the image at the position (i, j).

Texture features

Texture generally denotes the variations in the brightness of the pixel intensity in the image. The textual features are employed to divide the image into the region of interest. Texture features, like SLIF, PHOG, and LVP

SLIF: SLIF [61] is a feature descriptor that employs an exclusive description sampling template based on the spider's orb-web structure. It constructs a 2D orb-web sampling template for every identified key point based on the magnification factor, and spiral and radial thread counts. A set of vectors $S_7 = \{S_7^1, S_7^2, \ldots S_7^{\omega}\}$ corresponds to a set of target points $\{J_1, J_2, .., J_{\omega}\}$ in the image. Every point J_i is indicated by the characteristic scale ϑ_i and coordinate point . Initially, the orientation θ_i is assigned to every point $J_i \in J$ based on information sampling and web weight assignment technique. Later, an orb web structure OWS_i is defined for every point J_i. The web weights for all web nodes $(ma, mb)^i$. The SLIF feature vector S_7 is built by concatenating an 8-bit binary string series corresponding to the key point J_i in the web node $(ma, mb)^i$, and is given by,

$$S_{7i} = [O^i_{1,1}, O^i_{2,1}, \ldots, O^i_{MA,1}, O^i_{1,2}, O^i_{2,2}, \ldots, O^i_{MA,2}, O^i_{1,2}, O^i_{1,2}, \ldots, O^i_{MA,MB}] \tag{33}$$

Here, $O^i_{ma,mb}$ indicates an 8-bit binary array calculated for a specific web node $(ma, mb)^i$ in the orb web OWS_i.

PHOG: It [62] is a spatial-shape descriptor extensively employed in image processing. It is a vector notation that indicates the spatial distribution of the edges in the image. PHOG encompasses two portions, like pyramidal representation, and Histogram of Orientation Gradients (HOG), and is acquired by merging the HOG of all pyramid resolutions. PHOG is represented as

.

LVP: The LVP [63] feature is utilized for producing the most discriminative features in the image, and it provides multiple 2D spatial organization of micropatterns with varied vector direction combinations of the target and neighbouring pixels. This feature is enhanced Local Tetra Pattern (LTrP) that effectively reduces the feature length with the help of the Comparative Space Transform (CST) to encrypt the spatial relation of the neighbouring pixels with the target in four directions. LVP can be formulated as,

$$\begin{aligned} S_9 &= LVP_{\tau,\kappa}(V_i) \\ &= \{LVP_{\tau,\kappa,\varphi}(V_i) | \varphi = 0^\circ, 45^\circ, 90^\circ, 135^\circ\} \end{aligned} \tag{34}$$

where, V_i is the target pixel, τ represents the index of the adjacent pixel to V_i, κ designates the radius among the adjacent and target pixel, and φ is the index angle related to the directional change.

The feature thus generated are concatenated to obtain the feature vector, which is formulated as,

$$S = \{S_1, S_2, S_3, S_4, S_5, S_6, S_7, S_8, S_9\} \tag{35}$$

where, S_1 represents the CNN features, S_2 designates the mean, S_3 indicates variance, S_4 symbolizes standard deviation, S_5 refers to correlation, S_6 is the energy feature, S_7 labels SLIF, S_8 specifies PHOG, and the LVP feature is denoted by S_9. The feature vector S thus generated is then fed to the LeNet for classifying brain tumour.

Brain tumour classification

The classification process is employed to differentiate between the kinds of brain tumour: Gliomas, Meningiomas, and Pituitary tumours. The process is highly significant as the early prediction of tumour can substantially enhance the survival rate. The classification is carried out using the LeNet [64], The features

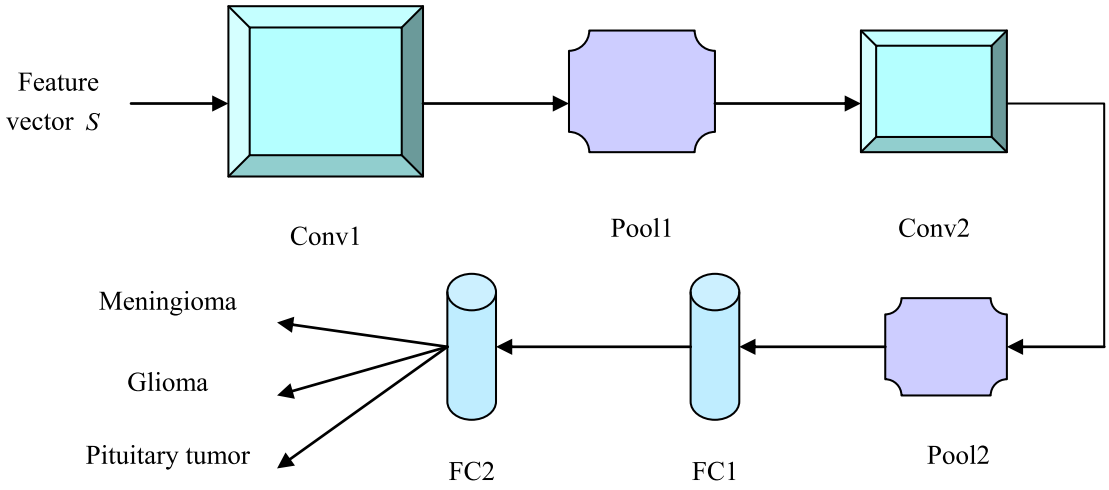

Figure 3. Structure of LeNet.

mined *S* from the segmented image are employed in the classification process. The weight parameters of the LeNet are critical as it contributes to an improved fitness measure. The optimal solution can be determined by performing weight optimization of the LeNet and this is executed based on the developed CAVO algorithm, which is developed by adapting the CAHA with respect to the AVOA [65] algorithm. The process of classification is elucidated in the subsequent sections.

Lenet structure

Classification is performed using the LeNet [64], which is applied to the feature vector *S* containing the most relevant features of the input image. LeNet-5 refers to LeCun's CNN, which was created to distinguish handwritten and printed characters. LeNet comprises conv, pooling, and FC layers. It has adequate inputs to acquire several objects and outputs, called Space Displacement Neural Networks (SDNN). The maxpool, and conv layers establish the lower layers, and the higher layer is formed using the FC layer link to Multi-Layer Perceptron (MLP). The lower layer produces a feature card set and is subjected to the first FC layer. Figure 3 exhibits the structure of the LeNet utilized for classifying brain tumour.

Training of LeNet with the presented CAVO algorithm

The training of LeNet includes determining the weights among the neurons in the LeNet to reduce the error. The weight optimization of LeNet using the developed CAVO algorithm has the ability to converge to the near-optimal or the best solution. The utilization of LeNet using the CAVO algorithm enhances the accuracy of classification. The CAVO algorithm is formulated by amending the optimization process of CAHA using the AVOA [65]. AVOA is a metaheuristic- algorithm formulated on the basis of the lifestyle, navigation, and foraging conduct of the African vultures. The implementation of the AVOA is executed in four phases: identifying the best vulture, starvation rate calculation, exploration, and exploitation. The AVOA has the ability to determine solutions with minimal computational burden and maximal flexibility. Further, it maintains a trade-off between resonance and variability. The adaptation of AVOA in CAHA effectively improves optimization efficiency. The devised CAVO algorithm is explained in the subsequent sections.

Fitness measure:

The optimal solution is attained by contemplating the solution that has the minimum fitness measure, wherein the fitness is computed using the expression below,

$$Fit = \frac{1}{\xi}\sum_{i=1}^{\xi}(Out_i - Out_i^*)^2 \tag{36}$$

Here, *Out* and *Out** indicate the output attained and the targeted output of the LeNet, and ξ represents the count of the training sample.

The final update equation of the CAHA is given by,

$$\begin{aligned} U_v(t+1) = \frac{1}{2}[&2U_{v,tar}(t)(1-\beta\cdot L)+\beta\cdot L\cdot U_v(t) \\ &+(1-\beta\cdot L)U_{v,tar}(t)+\beta^2\cdot L^2\cdot U_v(t-1)] \end{aligned} \tag{37}$$

From AVOA,

$$U_v(t+1) = I(t) - Da(t)\times F_a \tag{38}$$

$$Da(t) = |U\times I(t) - U_v(t)| \tag{39}$$

Here, F_a indicates the rate of satiation of the vulture and is found by,

$$F_a = (2\times rnd_1 + 1)\times z_a \times \left(1 - \frac{t}{t_{\max}}\right) + a_1 \tag{40}$$

Where, rnd_1 has an arbitrary value in the range [0, 1], z_a

and h_a are arbitrary numbers with value in the range $[-1, 1]$ and $[-2, 2]$ respectively.

Applying equation (39) in equation (38),

$$U_v(t+1) = I(t) - (|U \times I(t) - U_v(t)|) \times F_a \quad (41)$$

Consider, $I(t) > U_v(t)$, then

$$U_v(t+1) = I(t) - (U \times I(t) - U_v(t)) \times F_a \quad (42)$$

$$U_v(t+1) = I(t) - U \times I(t) \times F_a + U_v(t) \times F_a \quad (43)$$

$$U_v(t+1) = I(t)[1 - U \times F_a] + U_v(t) \times F_a \quad (44)$$

$$U_v(t) = \frac{U_v(t+1) - I(t)[1 - U \times F_a]}{F_a} \quad (45)$$

Substituting equation (45) in equation (37),

$$U_v(t+1) = \frac{1}{2}\left[\begin{array}{l} 2U_{v,tar}(t)(1-\beta\cdot L) + \beta\cdot L\cdot\left(\frac{U_v(t+1) - I(t)[1 - U\times F_a]}{F_a}\right) \\ +\beta\cdot L\cdot(1-\beta\cdot L)U_{v,tar}(t-1) + \beta^2\cdot L^2\cdot U_v(t-1) \end{array}\right] \quad (46)$$

$$U_v(t+1) - \frac{\beta\cdot L\cdot U_v(t+1)}{2F_a} = \frac{1}{2}\left[\begin{array}{l} 2U_{v,tar}(t)(1-\beta\cdot L) - \left(\frac{\beta\cdot L\cdot I(t)[1 - U\times F_a]}{F_a}\right) \\ +\beta\cdot L\cdot(1-\beta\cdot L)U_{v,tar}(t-1) + \beta^2\cdot L^2\cdot U_v(t-1) \end{array}\right] \quad (47)$$

$$\frac{2F_aU_v(t+1) - \beta\cdot L\cdot U_v(t+1)}{2F_a} = \frac{1}{2}\frac{\left[\begin{array}{l} 2U_{v,tar}(t)(1-\beta\cdot L)F_a - \beta\cdot L\cdot I(t)[1 - U\times F_a] \\ +\beta\cdot L\cdot(1-\beta\cdot L)U_{v,tar}(t-1)F_a + \beta^2\cdot L^2\cdot U_v(t-1)F_a \end{array}\right]}{F_a} \quad (48)$$

$$\begin{aligned}(2F_a - \beta\cdot L)\cdot U_v(t+1) &= 2U_{v,tar}(t)(1-\beta\cdot L)F_a - \beta\cdot L\cdot I(t)[1 - U\times F_a] \\ &+ \beta\cdot L\cdot(1-\beta\cdot L)U_{v,tar}(t-1)F_a + \beta^2\cdot L^2\cdot U_v(t-1)F_a\end{aligned} \quad (49)$$

$$U_v(t+1) = \frac{1}{(2F_a - \beta\cdot L)}\left[\begin{array}{l} F_a(2U_{v,tar}(t)(1-\beta\cdot L) + \beta\cdot L\cdot(1-\beta\cdot L)U_{v,tar}(t-1) + \beta^2\cdot L^2\cdot U_v(t-1)) \\ -\beta\cdot L\cdot I(t)[1 - U\times F_a] \end{array}\right] \quad (50)$$

Here, $U_v(t+1)$ symbolizes the location of the v^{th} solution at iteration, and signifies the location of the best solution.

Results and discussion

The results obtained during the experimentation of the formulated CAHA-CRF-CNN for tumour segmentation and the developed CAVO-LeNet for classifying brain tumours are depicted in this section with visual and numerical plots. Further, the performance of the devised technique is investigated based on several metrics by comparing it with conventional tumour detection techniques.

Experimental set-up

The devised CAVO-LeNet for classifying brain tumours is accomplished using a PC with Windows 10, 16 GB RAM, and Intel i3 processor within a MATLAB environment. Table 2 shows the parameter details of the proposed approach.

Table 2. Parameter details.

Parameter	Value
Learning rate	0.001
Batch size	32
epochs	30

Dataset description

The performance of any devised diagnosis scheme mostly depends on the database utilized for considering the problem to be addressed. Here, for detecting brain tumours, the MRI images are obtained from the most widely utilized images acquired from the Figshare dataset [67] and the Brain Tumour Segmentation (BRATS) 2018 dataset [68].

Figshare dataset: It comprises 3064 MRI images of the brain accumulated from 233 persons showing three different kinds of tumours, like glioma, pituitary, and meningioma. The MRI images acquired correspond to the T1-weighted contrast-enhanced modality. It encompasses a collection of 930 slices having the pituitary tumour, 1426 slices of glioma, as well as 708 slices of meningioma. The MRI images are stored in the.mat.

BRATS 2018 database: This database comprises 1024 MRI samples and facilities pre-operative MRI scans from multi-institutions and is utilized for performing the segmentation of brain tumours, including glioma. It also concentrates on predicting the endurance of the patients by evaluating the radiomic features.

Evaluation measures

The presented brain tumour classification approach is tested considering metrics, like accuracy, specificity, sensitivity, and ROC. These metrics are briefed in the subsequent sections.

Accuracy

Accuracy most significant parameter, which determines the total ratio of the input images that are exactly classified by the tumour detection technique, and is expressed as,

$$Acc = \frac{Pt + Nt}{Pt + Nt + Pf + Nf} \tag{51}$$

where, Pt is the total count of MRI images classified accurately as tumour, Nt implies the amount of images correctly classified as normal, Pf indicates the number of normal images identified as tumour, and Nf symbolizes cases of tumour categorized as normal.

Specificity

It gives the measure of the ratio of normal images distinguished correctly out of the total images classified as normal. Specificity is termed as a true negative rate and is computed using the following expression.

$$Specificity = \frac{Nt}{Nt + Pf} \tag{52}$$

Sensitivity

This parameter quantifies the number of input MRI images accurately classified as tumour out of the total cases of images classified as such. It is also referred as True Positive Rate (TPR) and is expressed as,

$$Sensitivity = \frac{Pt}{Pt + Nf} \tag{53}$$

ROC

ROC is a graph that depicts the effectiveness of the brain tumour classification scheme and is plotted based on the TPR and False Positive Rate (FPR). It depicts the performance of the classification technique in a curve form.

Experimental results

The image results obtained using the various processes, such as anisotropic filtering, tumour segmentation using CAHA-CRF-RNN, and feature extraction are portrayed considering BRATS 2018 and figshare databases, which is portrayed in Figure 4. Figure 4(a) displays the input image, Figure 4(b) depicts the filtered image, the segmented image is demonstrated in Figure 4(c), followed by the feature extraction images, like LVP in Figure 4(d) and PHOG in Figure 4(e). The first two rows indicate the image results attained using the BRATS 2018 dataset and the third and fourth rows specify the experimental outcomes using the figshare database.

Performance evaluation

The effectiveness of the proposed CAVO-LeNet is investigated by considering various measures, like accuracy, sensitivity, as well as specificity using images acquired from the figshare dataset and BRATS 2018 dataset, by considering different epochs, and this is elucidated in this section.

Evaluation using figshare dataset

This section details the assessment of the developed CAVO-LeNet using the figshare database based on different metrics, considering various swarm sizes. Figure 5(a) displays the performance valuation of the developed approach based on accuracy. With 60 epochs, the proposed CAVO-LeNet attained an accuracy of 0.824, 0.829, 0.858, 0.863, and 0.905, with a swarm size of 10, 20, 30, 40, and 50, correspondingly. Figure 5(b) illustrates the sensitivity-based investigation of the presented CAVO-LeNet. The value of sensitivity achieved by the CAVO-LeNet with 80 epochs is 0.819 with a swarm size of 10, 0.837 with a swarm size of 20, 0.850 with a swarm size of 30, 0.865 with a swarm size of 40, and 0.894 with a swarm size of 50. The valuation of the developed CAVO-LeNet, considering the specificity, is depicted in Figure 5(c). The presented CAVO-LeNet computed a specificity of 0.836, 0.856, 0.867, 0.882, and 0.918, with a swarm size of 10, 20, 30, 40, and 50, correspondingly, for 100 epochs.

Assessment based on BRATS 2018 dataset

The analysis of the presented CAVO-LeNet is also carried out by considering the BRATS 2018 dataset, which is exhibited in Figure 6. The accuracy-oriented valuation of the created CAVO-LeNet is portrayed in Figure 6(a). The accuracy computed, with 40 epochs, by the devised CAVO-LeNet is 0.823, 0.838, 0.848, 0.867, and 0.889, corresponding to a swarm size of 10, 20, 30, 40, and 50. In Figure 6(b), the analysis of the presented CAVO-LeNet with respect to the sensitivity parameter is displayed. The developed CAVO-LeNet attained a sensitivity value of 0.863 for swarm size of 10, 0.874 for swarm size of 20, 0.886 for swarm size of 30, 0.894 for swarm size of 40, and 0.905 for swarm size of 50, with 60 epochs. Figure 6(c) exhibits the performance valuation of the developed CAVO-LeNet considering specificity. The value of specificity value measured by the devised CAHO-LeNet for a swarm size of 10,

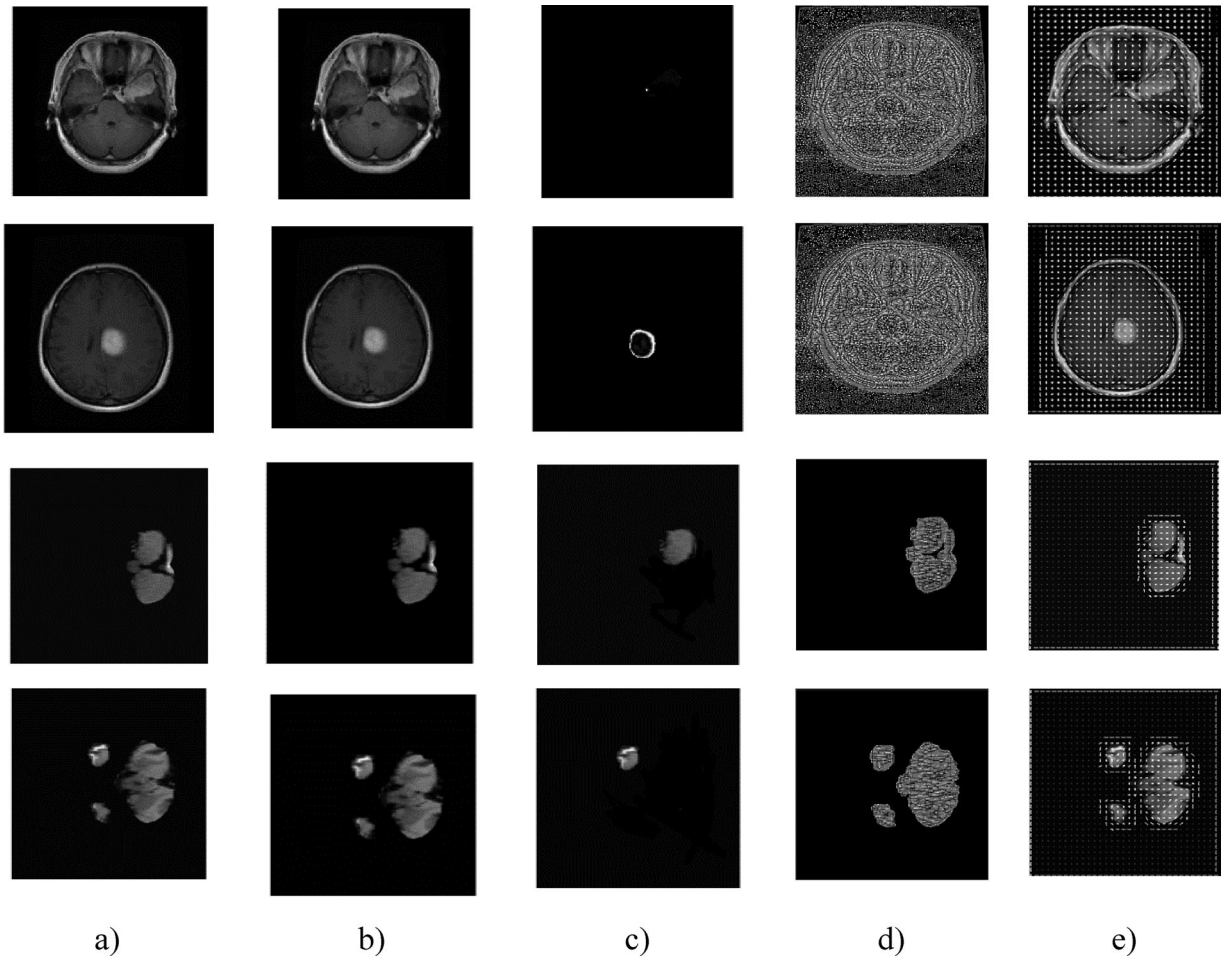

Figure 4. Image results obtained using the established CAVO-LeNet scheme for brain tumor detection (a) Input, (b) Filtered, (c) Segmented, (d) LVP, and (e) PHOG images.

20, 30, 40, and 50, is0.877, 0.884, 0.895, 0.898, and 0.915, respectively.

Segmentation assessment

The segmentation process distinguishes the growing tumour region in the brain from the normal areas, and here, a new segmentation technique is proposed using CAHA-CRF-RNN. This section evaluates the efficacy of the developed CAHA-CRF-RNN in comparison to the prevailing approaches, like Deep Joint segmentation [69], SegNet [70], and U-Net [71], considering the two datasets. Figure 7(a) illustrates the segmentation evaluation of the presented CAHA-CRF-RNN using the figshare dataset. The proposed CAHA-CRF-RNN computed a segmentation accuracy of 0.913 with a 60% learning set, which is better than the accuracies of 0.873, 0.831, and 0.832 attained by the segmentation approaches, like Deep Joint segmentation, SegNet, and U-Net. Figure 7(b) exhibits the segmentation analysis of the presented CAHA-CRF-RNN tumour segmentation using the BRATS 2018 database. With 80% learning set, the segmentation accuracy acquired by the techniques, like the devised CAHA-CRF-RNN, Deep Joint segmentation, SegNet, and U-Net is 0.919, 0.870, 0.866, and 0.851, which reveals a better performance.

Comparative techniques

The presented CAVO-LeNet for classifying brain tumour is tested for its effectiveness by comparing it with state-of-art techniques, such as Hybrid CNN-NADE [12], DLA [50], ELM-based Classifier [52], LSTM learning scheme [54], 3D CNN + CbFNN [49], K-means clustering + DWT [9], AVOA-LeNet, and AHA-LeNet.

Comparative assessment

The analysis is performed based on the images acquired from the figshare and the BRATS 2018 dataset, with respect to various measures, like accuracy, sensitivity, specificity, and ROC. Further, testing of the developed CAVO-LeNet is executed by considering different percentages of the learning set.

Analysis using figshare dataset

This section investigates the devised CAVO-LeNet, considering the images acquired from the figshare dataset. Figure 8(a) demonstrates the investigation of the

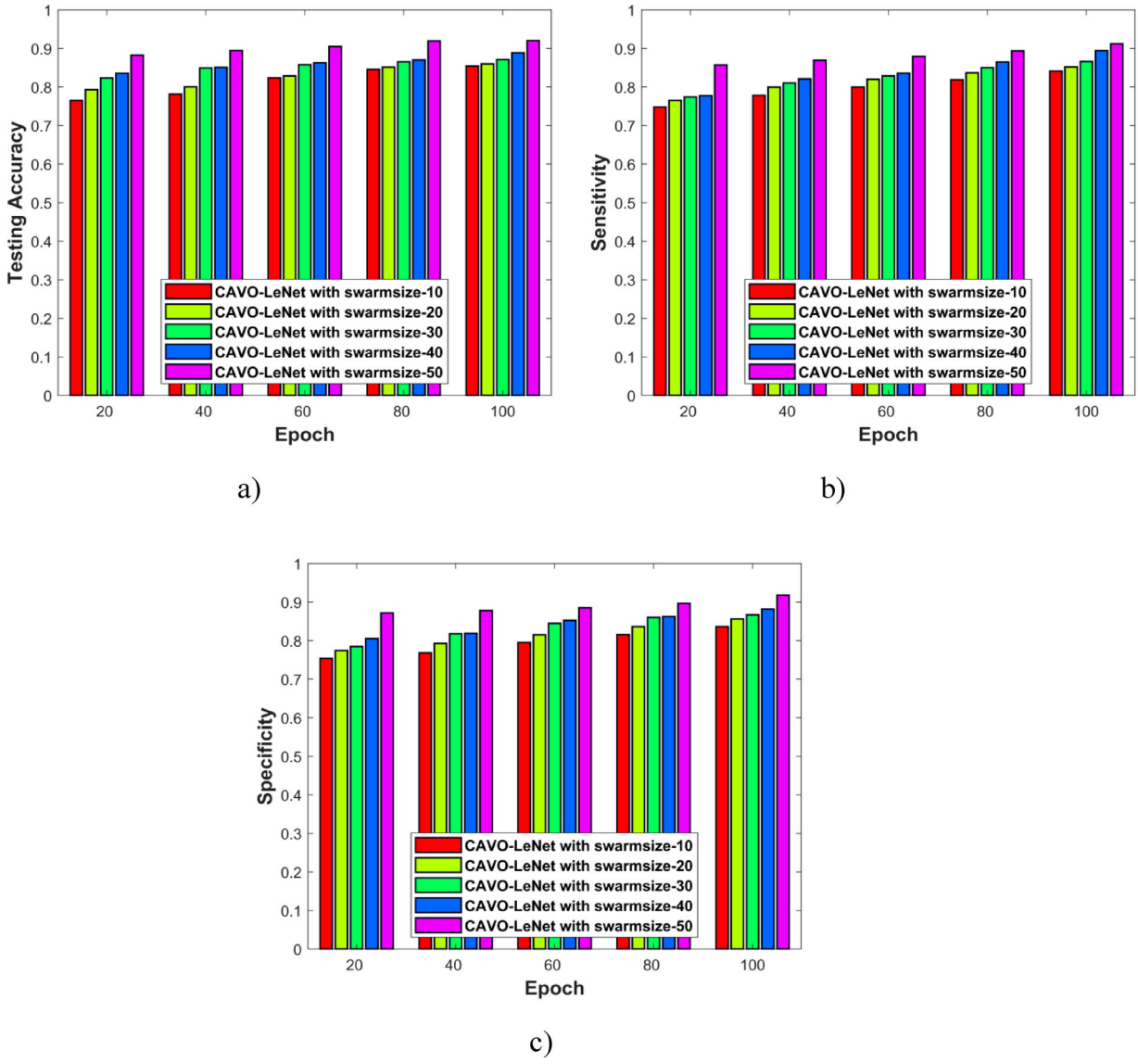

Figure 5. Assessment of the developed CAVO-LeNet considering (a) accuracy, (b) sensitivity, and (c) specificity using figshare database.

presented CAVO-LeNet considering accuracy. The accuracy value measured by the devised CAVO-LeNet is 0.920, for 80% learning set, and the accuracy value is high compared to the existing works. The accuracy calculated by the conventional schemes, such as Hybrid CNN-NADE, DLA, ELM-based Classifier, LSTM learning scheme, 3D CNN + CbFNN, K-means clustering + DWT, AVOA-LeNet, and AHA-LeNet is 0.803, 0.837, 0.867, 0.882, 0.819, 0.853, 0.876, and 0.891 and these produce a variation of 12.74%, 9.07%, 5.77%, 4.16%, 11%, 7.25%, 4.83%, and 3.20% in comparison to the current technique. The testing of the current work based on sensitivity using the figshare dataset is illustrated in Figure 8(b). The proposed CAVO-LeNet computes a sensitivity of 0.917, with 70% learning set. In contrast, the sensitivity values attained are 0.808 for Hybrid CNN-NADE, 0.838 for DLA, 0.841 for ELM-based Classifier, 0.878 for LSTM learning scheme, 0.8240 for 3D CNN + CbFNN, 0.8547 for K-means clustering + DWT, 0.8494 for AVOA-LeNet, and 0.8873 for AHA-LeNet. This depicts that the introduced CAVO-LeNet attained a higher sensitivity variation of 11.96%, 8.67%, 8.33%, 4.25%, 10.19%, 6.85%, 7.42%, and 3.29% concerning the available schemes. Figure 8(c) represents the investigation of the developed CAVO-LeNet based on the specificity parameter. For the 60% learning set, the specificity value calculated by the prevailing tumour classification methods, like Hybrid CNN-NADE, DLA, ELM-based Classifier, and LSTM learning scheme, 3D CNN + CbFNN, K-means clustering + DWT, AVOA-LeNet, and AHA-LeNet is 0.808, 0.832, 0.821, 0.877, 0.824, 0.849, 0.829, 0.885, and 0.917. The presented CAVO-LeNet figured a higher specificity of 0.917, thus producing a higher variation of 11.87%, 9.18%, 10.40%, 4.36%, 10.11%, 7.36%, 9.51%, and 3.41% with the specificity values of the existing techniques. The ROC-oriented evaluation of the proposed CAVO-LeNet is displayed in Figure 8(d). For a FPR of 0.7, the TPR value achieved by the Hybrid CNN-NADE, DLA, ELM-based Classifier,

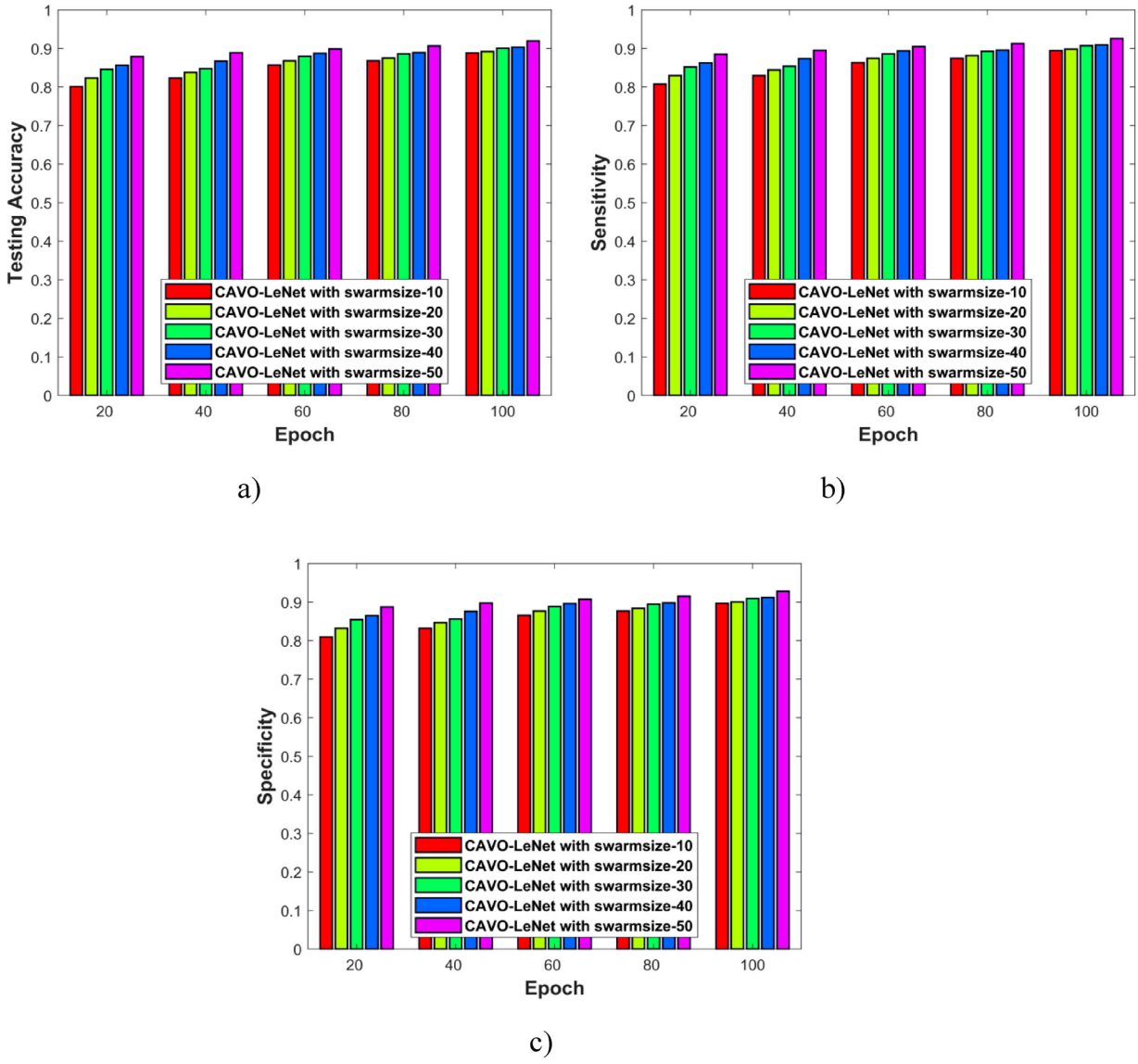

Figure 6. Examination of the presented CAVO-LeNet with respect to (a) accuracy, (b) sensitivity, and (c) specificity using BRATS 2018 database.

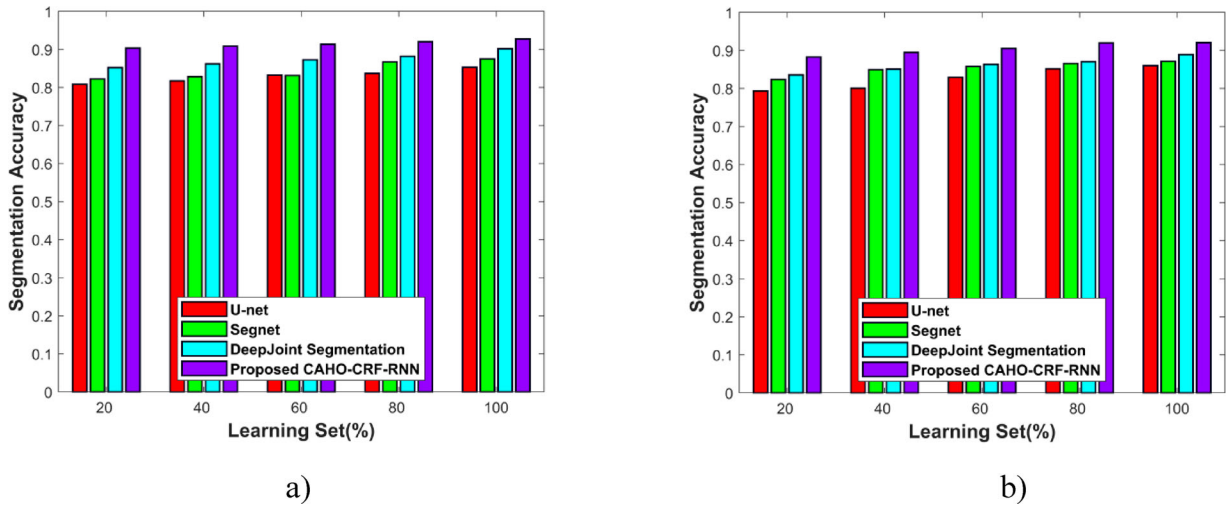

Figure 7. Segmentation analysis considering (a) figshare database, and (b) BRATS 2018 database.

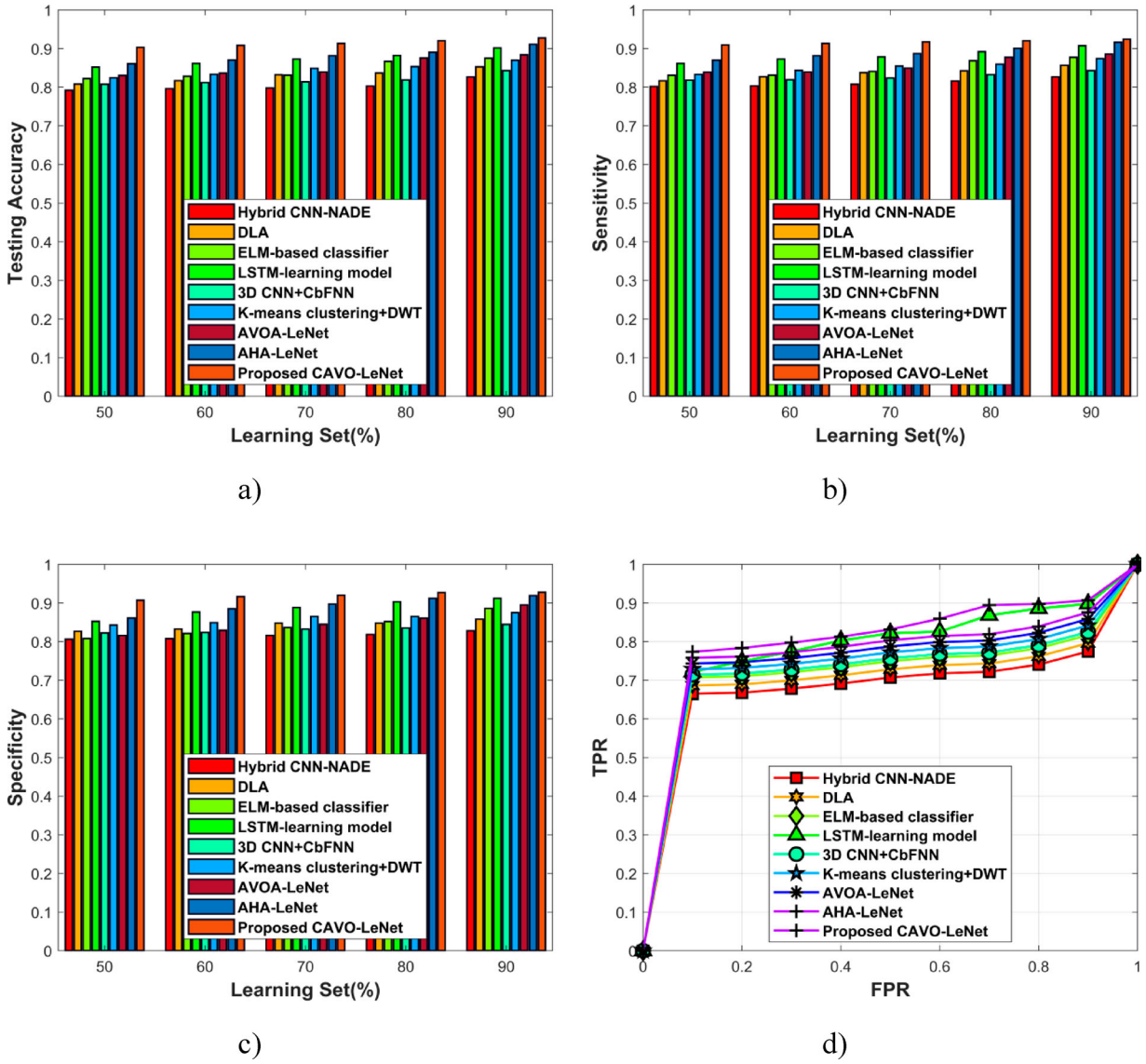

Figure 8. Valuation of the introduced CAVO-LeNet considering (a) accuracy, (b) sensitivity, (c) specificity and d) ROC considering figshare database.

LSTM learning scheme, 3D CNN + CbFNN, K-means clustering + DWT, AVOA-LeNet, and AHA-LeNet is 0.722, 0.743, 0.764, 0.868, 0.772, 0.787, 0.803, and 0.819. The current work, however, realized a higher value of TPR at 0.895.

Assessment based on BRATS 2018 dataset

This section presents the valuation of the effectiveness of the devised CAVO-LeNet considering the images acquired from BRATS 2018 dataset. The analysis of the developed approach corresponding to the accuracy parameter is portrayed in Figure 9 (a). The introduced CAVO-LeNet realized an accuracy value of 0.902, with 60% learning set, whereas the value of accuracy achieved by the traditional methods, such as Hybrid CNN-NADE is 0.829, DLA is 0.841, ELM-based Classifier is 0.852, LSTM learning scheme is 0.884, 3D CNN + CbFNN is 0.846, K-means clustering + DWT is 0.857, AVOA-LeNet is 0.860, and AHA-LeNet is 0.893. Hence, the presented CAVO-LeNet is found to have obtained a higher accuracy with a variation in values of 8.09%, 6.85%, 5.61%, 2.01%, 6.25%, 4.99%, 4.66%, and 1.03% with the prevailing methods. Figure 9(b) depicts the analysis of the current work based on sensitivity using the BRATS 2018 dataset. The current work realized a sensitivity of 0.918, while the available works, like Hybrid CNN-NADE, DLA, ELM-based Classifier, LSTM learning, 3D CNN + CbFNN, K-means clustering + DWT, AVOA-LeNet, and AHA-LeNet attained a lower value of 0.872, 0.883, 0.890, 0.891, 0.889, 0.900, 0.899, and 0.900 with 70% learning set. This shows that the current work has attained an improved sensitivity than the available schemes by producing a variation of 5.02%, 3.83%, 3.07%, 2.94%, 3.12%, 1.91%, 2.10%, and 1.97%. The developed CAVO-LeNet is investigated for its efficiency considering specificity, which is displayed in Figure 9(c). The prevailing techniques, like Hybrid CNN-NADE, DLA, ELM-based Classifier, LSTM learning method, 3D CNN + CbFNN, K-means

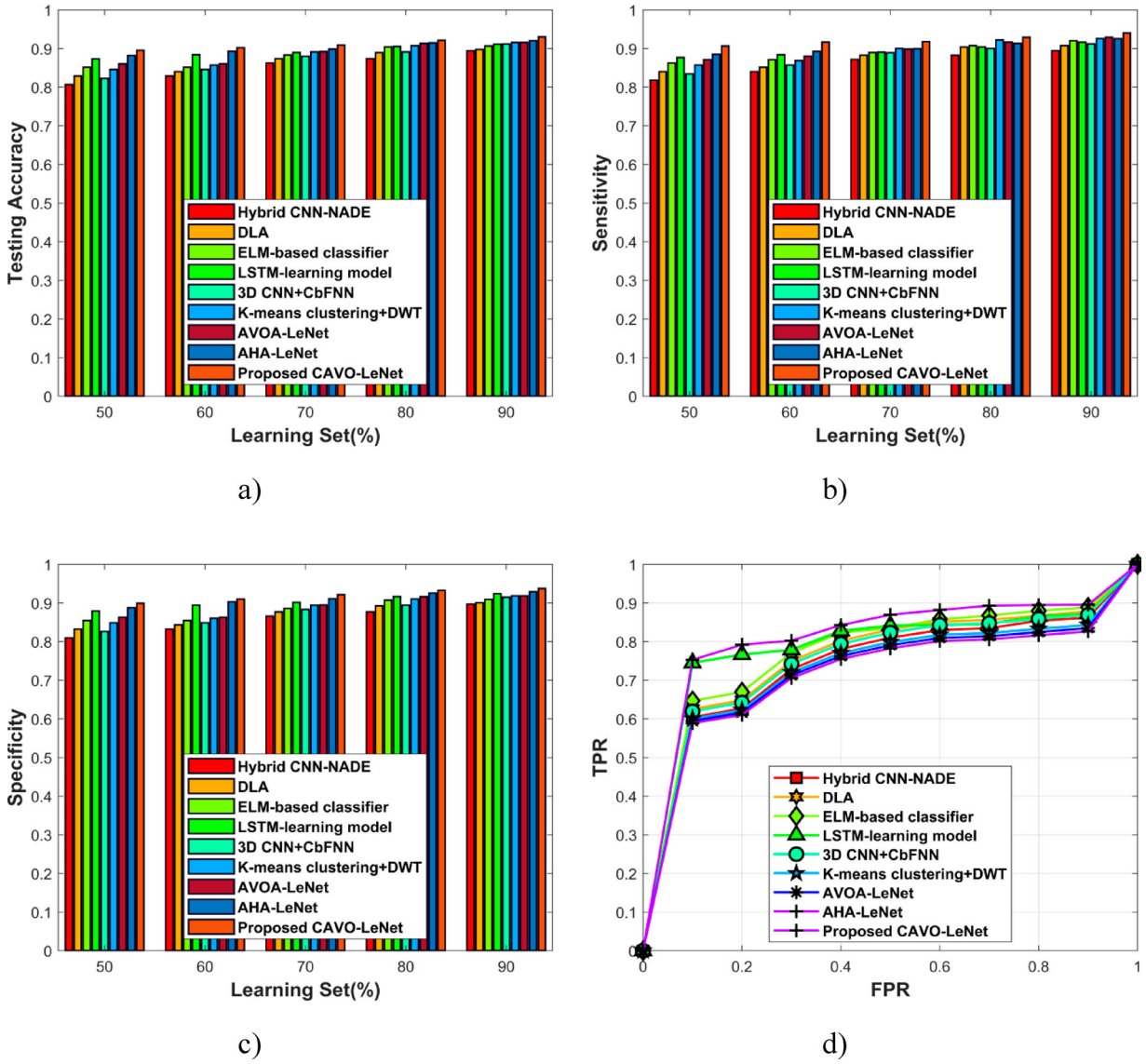

Figure 9. Analysis of the presented CAVO-LeNet using (a) accuracy, (b) sensitivity, (c) specificity, and (d) ROC based on the BRATS 2018 database.

clustering + DWT, AVOA-LeNet, and AHA-LeNet computed a specificity of 0.877, 0.893, 0.907, 0.917, 0.894, 0.910, 0.916, and 0.926. In contrast, the presented CAVO-LeNet realized a specificity of 0.933, with 80% learning set. This shows that the introduced CAVO-LeNet attained an enhanced variation in specificity by 6.02%, 4.34%, 2.77%, 1.77%, 4.15%, 2.42%, 1.79%, and 0.79% corresponding to the prevailing methods. Figure 9(d) depicts the assessment of the introduced CAVO-LeNet considering the ROC. The value of TPR computed by the existing tumour detection methodologies, like Hybrid CNN-NADE is 0.830, DLA is 0.851, ELM-based Classifier is 0.857, LSTM learning method is 0.843, 3D CNN + CbFNN is 0.843, K-means clustering + DWT is 0.818, AVOA-LeNet is 0.809, and AHA-LeNet is 0.801 with FPR of 0.6, while the current work attained a TPR of 0.882.

Table 3. Comparative discussion of the devised CAVO-LeNet for classifying brain tumor.

Metrics	Hybrid CNN-NADE	DLA	ELM-based classifier	LSTM learning model	3D CNN + CbFNN	K-means clustering + DWT	AVOA-LeNet	AHA-LeNet	Proposed CAVO-LeNet
Figshare dataset									
Sensitivity	0.827	0.857	0.877	0.907	0.843	0.874	0.886	0.916	0.925
Accuracy	0.826	0.853	0.875	0.902	0.843	0.870	0.884	0.911	0.928
Specificity	0.828	0.858	0.886	0.912	0.845	0.875	0.895	0.919	0.928
BRATS 2018 dataset									
Sensitivity	0.894	0.908	0.920	0.917	0.912	0.926	0.929	0.926	**0.941**
Accuracy	0.894	0.898	0.907	0.911	0.912	0.916	0.916	0.920	**0.930**
Specificity	0.897	0.901	0.910	0.924	0.915	0.919	0.919	0.929	**0.938**

Table 4. Statistical analysis.

Methods	Sensitivity			Accuracy			Specificity		
	Best	Mean	Variance	Best	Mean	Variance	Best	Mean	Variance
Figshare dataset									
Hybrid CNN-NADE	0.827	0.824	0.003	0.826	0.823	0.003	0.828	0.824	0.004
DLA	0.857	0.853	0.004	0.853	0.850	0.003	0.858	0.853	0.005
ELM-based classifier	0.877	0.874	0.003	0.875	0.871	0.004	0.886	0.882	0.004
LSTM learning model	0.907	0.903	0.004	0.902	0.900	0.002	0.912	0.909	0.003
3D CNN + CbFNN	0.843	0.840	0.003	0.843	0.840	0.003	0.845	0.840	0.005
K-means clustering + DWT	0.874	0.870	0.004	0.870	0.866	0.004	0.875	0.871	0.004
AVOA-LeNet	0.886	0.883	0.003	0.884	0.880	0.004	0.895	0.892	0.003
AHA-LeNet	0.916	0.912	0.004	0.911	0.909	0.002	0.919	0.915	0.004
Proposed CAVO-LeNet	0.925	0.923	0.002	0.928	0.926	0.002	0.928	0.926	0.002
BRATS 2018 dataset									
Hybrid CNN-NADE	0.894	0.890	0.004	0.894	0.890	0.004	0.897	0.894	0.003
DLA	0.908	0.904	0.004	0.898	0.895	0.003	0.901	0.898	0.003
ELM-based Classifier	0.920	0.915	0.005	0.907	0.904	0.003	0.910	0.907	0.003
LSTM learning Model	0.917	0.914	0.003	0.911	0.908	0.003	0.924	0.920	0.004
3D CNN + CbFNN	0.912	0.909	0.003	0.912	0.909	0.003	0.915	0.912	0.003
K-means clustering + DWT	0.926	0.922	0.004	0.916	0.913	0.003	0.919	0.914	0.005
AVOA-LeNet	0.929	0.926	0.003	0.916	0.912	0.004	0.919	0.917	0.002
AHA-LeNet	0.926	0.923	0.003	0.920	0.916	0.004	0.929	0.926	0.003
Proposed CAVO-LeNet	0.941	0.939	0.002	0.930	0.928	0.002	0.938	0.937	0.001

Comparative discussion

The efficiency of the presented CAVO-LeNet for classifying brain tumour is assessed by comparing it with the available approaches in brain tumour diagnosis based on the images acquired from the figshare and BRATS 2018 datasets. Further, the assessment is accomplished by taking into account various parameters, like sensitivity, accuracy, as well as specificity. The comparison of the current work with respect to the existing schemes is exhibited in Table 3, with the values displayed associated with the learning set of 90%. It can be inferred that the devised CAVO-LeNet technique realized a higher value of sensitivity of 0.941, accuracy of 0.930, and specificity of 0.938. The process of segmentation using the CAHA-CRF-RNN accounts for the enhanced accuracy, and the sensitivity is enhanced by the usage of LeNet for classification, and the optimization of LeNet with the CAVO algorithm improves the specificity.

Statistical analysis

Table 4 shows the statistical analysis of the suggested CAVO-LeNet and the existing methods based on the evaluation metrics. The statistical analysis is evaluated by considering best, mean, and variance.

Conclusion

This paper presents a highly efficient method for identifying brain tumour from MRI images of the brain. The main contribution of the current work is two-fold; an improved segmentation technique and a novel classification scheme. A tumour segmentation approach is presented for distinguishing the growing tumour area in the brain from the normal areas using the CRF-RNN, which is tuned using the devised CAHA. Further, a new approach for categorizing brain tumour is proposed, wherein the image is classified as meningiomas, gliomas, or pituitary tumour. Classification is accomplished using the LeNet, with weight optimization performed by the proposed CAVO algorithm. Moreover, the efficacy of the devised CAVO-LeNet is investigated, considering measures like sensitivity, accuracy, specificity, and ROC, and is observed to have attained higher values of sensitivity, accuracy, and specificity at 0.941, 0.930, and 0.938. The proposed method is employed for identifying in brain tumours in the early stages. Also, it helps in appropriate treatment, and the survival rate of the affected individuals can be prolonged. The utilization of anisotropic filtering limits the efficiency of this work, as the filter suffers from a reduced Peak Signal to Noise Ratio (PSNR) in case of images with high noise intensities (more than 3% of the maximal intensity), thus failing to preserve the edges, and this issue will be focussed in the future.

Disclosure statement

No potential conflict of interest was reported by the author(s).

Notes on contributors

Dr. Geetha M Working as Professor in the Department of Computer Science and Engineering, Chennai Institute of Technology, Chennai, Tamil Nadu, India, having 24 Years of experience in Teaching, and has obtained her under graduate degree B.E from Bharathidasan University, Tamil Nadu, India, and Post graduate degree M.E from Satyabhama Institute of Science and Technology. Chennai, Tamil Nadu, India. She completed her Ph.D. degree from Anna University, Chennai, Tamil Nadu, India, in the area of Pervasive Computing. Her main research interests are Automata Theory, Information Security, Machine Learning and Computational Linguistics. Apart from these, her research interests also include Edge Computing and Internet of Things. She has published her papers in more than 50 refereed Journals and also written a book chapter "Biomedical Data Mining

for Improved Clinical Diagnosis" in Artificial Intelligence in Data Mining, Elsevier Inc, 2021.

Dr Prasanna Lakshmi K, earned her Doctorate in Computer Science and Engineering from Jawaharlal Nehru Technological University, Hyderabad, Master Degree in Computer Science and Engineering from Osmania University, Hyderabad. She is currently working as Professor in Information Technology Department, Gokaraju Rangaraju Institute of Engineering and Technology, Hyderabad. She has more than 20 years of Teaching Experience and 4 years of Research Experience. Published 32 research publications in reputed journals which are indexed in Web of Science and Scopus. Guided 9 PG projects and 15 UG projects. She published 1 Indian Patent and been granted with 1 Australian Patent. An active member in Advisory Board Committee for many International Conferences organized through IEEE. Reviewed more than 100 manuscripts being a member of Technical Review Committee in various renowned journals and conferences.Awarded with Global Eminent Teacher award in 2021 and with 50 Fabulous EduTech Leaders award in 2019. She has professional memberships from IACSIT, IAENG and CSTA. Apart from research activities, she also served the institution in many administrative roles like Member Secretary for Academic Council, Chairman Board of Studies, Head of Information Technology Department and Dean of Faculty Development in GRIET. Currently serving Institution with Dean Academics role. Implemented OBE based teaching in classroom. Her research interests include Data Stream Mining, Machine Learning, Natural Language Processing, IoT and Social Networking.

Prof. Sajeev Ram Arumugam is currently associated with Sri Krishna College of Engineering and Technology as Associate Professor in Department of Artificial Intelligence and Data Science. He was graduated in B.E.ECE in 2007 followed by M,E CSE in the year 2011 and completed his Ph.D from Vels Institute of Science, Technology & Advanced Studiesin 2019. Prof. Sajeev have authored more than 20+ research articles and Book Chapters in the field of medical image processing, Deep Learning, IoT. He have also participated in 10+ national and international conferences. He is also associated with many journals and have peer reviewed 10+articles for 3 journals. He have authored 2 books, and his research interest includes developing Computer Aided Detection systems in medical fields using Machine and Deep Learning Algorithms, and Developing IoT based AI systems in various fields.

Dr. Sandhya N currently works at VNR Vignana Jyothi Institute of Engineering and Technology. Her research area is Data Science. She has published around 30 papers in reputed international journals and presented papers at international conferences. She has an experience of 18 years in teaching and administration. Her scholars are working on text mining, big data analytics and sentiment mining.

References

[1] Chen Y, Schönlieb CB, Liò P, et al. AI-based reconstruction for fast MRI – a systematic review and meta-analysis. Proc IEEE. 2022;110(2):224–245.

[2] Hollingsworth KG. Reducing acquisition time in clinical MRI by data undersampling and compressed sensing reconstruction. Phys Med Biol. 2015;60(21):R297.

[3] Roy S, Bhattacharyya D, Bandyopadhyay SK, et al. An effective method for computerized prediction and segmentation of multiple sclerosis lesions in brain MRI. Comput Methods Programs Biomed. 2017;140:307–320.

[4] Roy S, Bandyopadhyay SK. Abnormal regions detection and quantification with accuracy estimation from MRI of brain. In the Proceeding of 2nd International Symposium on Instrumentation and Measurement, Sensor Network and Automation (IMSNA). IEEE, Toronto, ON, Canada, 2013.

[5] Gangopadhyay T, Halder S, Dasgupta P, et al. MTSE U-Net: an architecture for segmentation, and prediction of fetal brain and gestational age from MRI of brain. Netw Model Anal Health Inform Bioinform. 2022;11.

[6] Roy S, Bhattacharyya D, Bandyopadhyay SK, et al. An iterative implementation of level set for precise segmentation of brain tissues and abnormality detection from MR images. IETE J Res. 2017;63(6):769–783.

[7] Roy S, KumarBandyopadhyay S. A new method of brain tissues segmentation from MRI with accuracy estimation. Proc Comput Sci. 2016;85:362–369.

[8] Rammurthy D, Mahesh PK. Whale Harris hawks optimization based deep learning classifier for brain tumor detection using MRI images. J King Saud Univ Comp Inform Sci. 2020;34:3259–3272.

[9] Chaudhary A, Bhattacharjee V. An efficient method for brain tumor detection and categorization using MRI images by K-means clustering & DWT. Int J Inf Technol . 2020;12(1):141–148.

[10] Amin J, Sharif M, Yasmin M, et al. A distinctive approach in brain tumor detection and classification using MRI. Pattern Recognit Lett. 2020;139:118–127.

[11] Harish P, Baskar S. MRI based detection and classification of brain tumor using enhanced faster R-CNN and Alex Net model. Mater Today Proc. 2020.

[12] Hashemzehi R, Mahdavi SJS, Kheirabadi M, et al. Detection of brain tumors from MRI images base on deep learning using hybrid model CNN and NADE. Biocybern Biomed Eng. 2020;40(3):1225–1232.

[13] Saba T, Mohamed AS, El-Affendi M, et al. Brain tumor detection using fusion of hand crafted and deep learning features. Cogn Syst Res. 2020;59:221–230.

[14] Gali V. A novel robust controller of drug dosage for cancer chemotherapy. J Comput Mech Power Syst Contr. 2021;4:2.

[15] Ganeshan R. Skin cancer detection with optimized neural network via hybrid algorithm. Multimedia Res. 2020;3:2.

[16] Khan R. Artificial bee colony-based general adversarial network for liver cancer detection using CT images. Multimedia Res. 2020;3:4.

[17] Khan MA, Lali IU, Rehman A, et al. Brain tumor detection and classification: A Framework of marker–based watershed algorithm and multilevel priority features selection. Microsc Res Techn. 2019;82(6):909–922.

[18] Khushi M, Shaukat K, Alam TM, et al. A comparative performance analysis of data resampling methods on imbalance medical data. IEEE Access. 2021;9:109960–109975.

[19] Naseem U, Khushi M, Khan SK, et al. A comparative analysis of active learning for biomedical text mining. Appl Syst Innov. 2021;4:1.

[20] Li M, Kuang L, Xu S, et al. Brain tumor detection based on multimodal information fusion and convolutional neural network. IEEE Access. 2019;7:180134–180146.

[21] Alam TM, Shaukat K, Khan WA, et al. An efficient deep learning-based skin cancer classifier for an imbalanced dataset. Diagnostics. 2022;12:9.

[22] Alam TM, Shaukat K, Khelifi A, et al. A fuzzy inference-based decision support system for disease diagnosis. Comput J. 2022.

[23] Yang X, Khushi M, Shaukat K. Biomarker CA125 feature engineering and class imbalance learning improves ovarian cancer prediction. In: The Proceeding of IEEE Asia-Pacific Conference on Computer Science and Data Engineering (CSDE), IEEE, Gold Coast, Australia, 2020.
[24] Bilal A, Sun G, Mazhar S, et al. Improved grey wolf optimization-based feature selection and classification using CNN for diabetic retinopathy detection. Evol Comp Mobile Sustain Netw. 2022;116:1–14.
[25] Bilal A, Sun G, Mazhar S. Finger-vein recognition using a novel enhancement method with convolutional neural network. J Chin Inst Eng . 2021;44(5):407–417.
[26] Bilal A, Sun G, Mazhar S. Diabetic retinopathy detection using weighted filters and classification using CNN. In: The proceeding of International Conference on Intelligent Technologies (CONIT), IEEE, Hubli, India, 2021.
[27] Bilal A, Zhu L, Deng A, et al. AI-based automatic detection and classification of diabetic retinopathy using U-Net and deep learning. Symmetry. 2022;14(7):1–19.
[28] Bilal A, Sun G, Li Y, et al. Lung nodules detection using weighted filters and classification using CNN. J Chin Inst Eng . 2022;45(2):175–186.
[29] Bilal A, Sun G, Mazhara S, et al. A transfer learning and U-Net-based automatic detection of diabetic retinopathy from fundus images. Comp Meth Biomech Biomed Eng Imag Visual. 2022;10(6):663–674.
[30] Garg G, Garg R. Brain tumor detection and classification based on hybrid ensemble classifier. arXiv preprint arXiv:2101.00216, 2021.
[31] Bilal A, Sun G, Mazhar S. Survey on recent developments in automatic detection of diabetic retinopathy. J Franç Ophtal. 2021;44(3):420–440.
[32] Bilal A, Sun G, Li Y, et al. Diabetic retinopathy detection and classification using mixed models for a disease grading database. IEEE Access. 2021;9:23544–23553.
[33] Bonte S, Goethals I, Van RH. Machine learning based brain tumour segmentation on limited data using local texture and abnormality. Comput Biol Med. 2018;98:39–47.
[34] Shaukat K, Luo S, Chen S, et al. Cyber threat detection using machine learning techniques: a performance evaluation perspective. In: The proceeding of International Conference on Cyber Warfare and Security (ICCWS), IEEE, Islamabad, Pakistan, 2020.
[35] Elaff I. Comparative study between spatio-temporal models for brain tumor growth. Biochem Biophys Res Commun 2018;496(4):1263–1268.
[36] Ananthi VP, Balasubramaniam P, Kalaiselvi T. A new fuzzy clustering algorithm for the segmentation of brain tumor. Soft Comput. 2016;20(12):4859–4879.
[37] Wu W, Chen AYC, Zhao L. Brain tumor detection and segmentation in a CRF framework with pixel-pairwise affinity and super pixel-level features. Int J Comput Assist Radiol Surg. 2014;9(2):241–253.
[38] Bilal A, Sun G. Neuro-optimized numerical solution of non-linear problem based on Flierl–Petviashivili equation. SN Appl Sci. 2020;2:7.
[39] Bilal A, Sun G, Mazhar S, et al. Neuro-optimized numerical treatment of HIV infection model. Int J Biomath. 2021;14:5.
[40] Roy S, Meena T, Lim S-J. Demystifying supervised learning in healthcare 4.0: a new reality of transforming diagnostic medicine. Diagnostics. 2022;12:10.
[41] Devnath L, Luo S, Summons P, et al. Deep ensemble learning for the automatic detection of pneumoconiosis in coal worker's chest X-ray radiography. J Clin Med. 2022;11:18.
[42] Shaukat K, Luo S, Varadharajan V. A novel method for improving the robustness of deep learning-based malware detectors against adversarial attacks. Eng Appl Artif Intell. 2022;116.
[43] Dar KS, Luo S, Varadharajan V, et al. Performance comparison and current challenges of using machine learning techniques in cybersecurity. Energies. 2020;13:10.
[44] Shaukat K, Luo S, Varadharajan V, et al. A survey on machine learning techniques for cyber security in the last decade. IEEE Access. 2020;8:222310–222354.
[45] Luo S, Shaukat K. Computational methods for medical and cyber security. In: *Book: Applied sciences*, 2022. p. 1–228.
[46] Rehman A, Naz S, Razzak MI, et al. A deep learning-based framework for automatic brain tumors classification using transfer learning. Circ Syst Signal Process. 2020;39(2):757–775.
[47] Gopal A. Hybrid classifier: brain tumor classification and segmentation using genetic-based grey wolf optimization. Multimed Res. 2020;3:2.
[48] Gokulkumari G. Classification of brain tumor using Manta Ray foraging optimization-based DeepCNN classifier. Multimed Res. 2020;3:4.
[49] Rehman A, Khan MA, Saba T, et al. Microscopic brain tumor detection and classification using 3D CNN and feature selection architecture. Microsc Res Tech. 2021;84(1):133–149.
[50] Rajinikanth V, Joseph Raj AN, Thanaraj KP, et al. A customized VGG19 network with concatenation of deep and handcrafted features for brain tumor detection. Appl Sci. 2020;10(10):3429.
[51] Srinivas C, Prasad N, Zakariah M, et al. Deep transfer learning approaches in performance analysis of brain tumor classification using MRI images. J Healthc Eng. 2022;2:1–17.
[52] Sharif M, Amin J, Raza M, et al. Brain tumor detection based on extreme learning. Neural Comp Appl. 2020;32(20):15975–15987.
[53] Deb D, Roy S. Brain tumor detection based on hybrid deep neural network in MRI by adaptive squirrel search optimization. Multimed Tools Appl. 2021;80(2):2621–2645.
[54] Amin J, Sharif M, Raza M, et al. Brain tumor detection: a long short-term memory (LSTM)-based learning model. Neural Comp Appl. 2020;32(20):15965–15973.
[55] Sharma AK, Nandal A, Dhaka A, et al. Enhanced watershed segmentation algorithm-based modified ResNet50 model for brain tumor detection. BioMed Res Int. 2022;1:1–14.
[56] Bilenia A, Sharma D, Raj H, et al. Brain tumor segmentation with skull stripping and modified fuzzy C-means. In: Information and communication technology for intelligent systems. Singapore: Springer; 2019. p. 106: 229–237.
[57] Wang S, Yi L, Chen Q, et al. Edge-aware fully convolutional network with CRF-RNN layer for hippocampus segmentation. In: The proceedings of 2019 IEEE 8th Joint International Information Technology and Artificial Intelligence Conference (ITAIC). IEEE, 2019. p. 803–806.
[58] Zhao W, Wang L, Mirjalili S. Artificial hummingbird algorithm: a new bio-inspired optimizer with its

engineering applications. Comput Methods Appl Mech Eng. 2022;388:114194.
[59] Su R, Liu T, Sun C, et al. Fusing convolutional neural network features with hand-crafted features for osteoporosis diagnoses. Neurocomputing. 2020;385:300–309.
[60] Iqbal N, Mumtaz R, Shafi U, et al. Gray level co-occurrence matrix (GLCM) texture based crop classification using low altitude remote sensing platforms. PeerJ Comp Sci. 2021;7:e536.
[61] Fausto F, Cuevas E, Gonzales A. A new descriptor for image matching based on bionic principles. Pattern Anal Appl. 2017;20(4):1245–1259.
[62] Bai Y, Guo L, Jin L, et al. A novel feature extraction method using pyramid histogram of orientation gradients for smile recognition. In: The proceedings of IEEE 16th International Conference on Image Processing (ICIP), November 2009. p. 3305–3308.
[63] Fan KC, Hung TY. A novel local pattern descriptor – local vector pattern in high-order derivative space for face recognition. IEEE Trans Image Process. 2014;23(7):2877–2891.
[64] Sarraf S, Tofighi G. Classification of Alzheimer's disease using FMRI data and deep learning convolutional neural networks. arXiv preprint arXiv:1603.08631, 2016.
[65] Abdollahzadeh B, Gharehchopogh FS, Mirjalili S. African vultures optimization algorithm: a new nature-inspired metaheuristic algorithm for global optimization problems. Comput Ind Eng. 2021;158:107408.
[66] Zheng S, Jayasumana S, Romera-Paredes B, et al. Conditional random fields as recurrent neural networks. In Proceedings of the IEEE international conference on computer vision, 2015. p. 1529–1537.
[67] Figshare dataset. [cited 2022 Sep] available at https://figshare.com/articles/brain_tumor_dataset/1512427.
[68] BRATS 2018 database. [cited 2022 Sep] available at https://wiki.cancerimagingarchive.net/pages/viewpage.action?pageId=37224922.
[69] Renjit A. Deepjoint segmentation for the classification of severity-levels of glioma tumour using multimodal MRI images. IET Image Proc. 2020;14(11):2541–2552.
[70] Badrinarayanan V, Kendall A, Cipolla R. Segnet: a deep convolutional encoder-decoder architecture for image segmentation. IEEE Trans Pattern Anal Mach Intell. 2017;39(12):2481–2495.
[71] Ronneberger O, Fischer P, Brox T. U-net: convolutional networks for biomedical image segmentation. In: Proceedings of international conference on medical image computing and computer-assisted intervention. Cham: Springer; 2015. p. 234–241.